The Astrophysical Journal Supplement Series, 221:29 (25pp), 2015 December doi:10.1088/0067-0049/221/2/29

DARK MATTER SEARCHES IN THE GAMMA-RAY EXTRAGALACTIC BACKGROUND VIA CROSS-CORRELATIONS WITH GALAXY CATALOGS

Alessandro Cuoco[1,2], Jun-Qing Xia[3,4], Marco Regis[1,2], Enzo Branchini[5,6,7], Nicolao Fornengo[1,2], and Matteo Viel[8,9]
[1] Dipartimento di Fisica, Università di Torino, via P. Giuria 1, I-10125 Torino, Italy; cuoco@to.infn.it, regis@to.infn.it, fornengo@to.infn.it
[2] Istituto Nazionale di Fisica Nucleare, Sezione di Torino, via P. Giuria 1, I-10125 Torino, Italy
[3] Department of Astronomy, Beijing Normal University, Beijing 100875, China; xiajq@bnu.edu.cn
[4] Key Laboratory of Particle Astrophysics, Institute of High Energy Physics, Chinese Academy of Science, P.O. Box 918-3, Beijing 100049, P. R. China
[5] Dipartimento di Matematica e Fisica, Università degli Studi "Roma Tre," via della Vasca Navale 84, I-00146 Roma, Italy; branchin@fis.uniroma3.it
[6] INFN, Sezione di Roma Tre, via della Vasca Navale 84, I-00146 Roma, Italy
[7] INAF Osservatorio Astronomico di Roma, Osservatorio Astronomico di Roma, Monte Porzio Catone, Italy
[8] INAF Osservatorio Astronomico di Trieste, Via G. B. Tiepolo 11, I-34141, Trieste, Italy; viel@oats.inaf.it
[9] INFN, Sezione di Trieste, via Valerio 2, I-34127, Trieste, Italy
Received 2015 June 2; accepted 2015 November 2; published 2015 December 7

ABSTRACT

We compare the measured angular cross-correlation between the *Fermi*-Large Area Telescope γ-ray sky and catalogs of extragalactic objects with the expected signal induced by weakly interacting massive particle (WIMP) dark matter (DM). We include a detailed description of the contribution of astrophysical γ-ray emitters such as blazars, misaligned active galactic nucleus (AGN), and star-forming galaxies, and perform a global fit to the measured cross-correlation. Five catalogs are considered: Sloan Digital Sky Survey (SDSS)-DR6 quasars, Two Micron All Sky Survey galaxies, NRAO VLA Sky Survey radio galaxies, SDSS-DR8 Luminous Red Galaxies, and the SDSS-DR8 main galaxy sample. To model the cross-correlation signal, we use the halo occupation distribution formalism to estimate the number of galaxies of a given catalog in DM halos and their spatial correlation properties. We discuss uncertainties in the predicted cross-correlation signal arising from the DM clustering and WIMP microscopic properties, which set the DM γ-ray emission. The use of different catalogs probing objects at different redshifts significantly reduces, though not completely, the degeneracy among the different γ-ray components. We find that the presence of a significant WIMP DM signal is allowed by the data but not significantly preferred by the fit, although this is mainly due to a degeneracy with the misaligned AGN component. With modest substructure boost, the sensitivity of this method excludes thermal annihilation cross sections at 95% level for WIMP masses up to few tens of GeV. Constraining the low-redshift properties of astrophysical populations with future data will further improve the sensitivity to DM.

Key words: cosmology: observations – cosmology: theory – dark matter – gamma-rays: diffuse backgrounds – large-scale structure of universe

1. INTRODUCTION

The last few years have seen a tremendous improvement in our understanding of the γ-ray sky, mostly due to the observations performed by the Large Area Telescope (LAT) on board of the *Fermi* satellite (Atwood et al. 2009). Among the main issues that have been investigated, an important one is the understanding of the origin of the Isotropic Gamma-Ray Background (IGRB; Ackermann et al. 2015a; Fornasa & Sanchez-Conde 2015), i.e., the fraction of the extragalactic γ-ray background (EGB) that has not been resolved into individual sources. The nature of the extragalactic emission is a recurrent issue which arises each time a new observational window of the electromagnetic spectrum is opened on the universe. A good example is the quest for the origin of the soft X-ray background, with the important difference that the latter has now been largely resolved (see, e.g., Hickox & Markevitch 2007), whereas a significant fraction of the γ-ray flux is still diffuse, leaving room for potential new discoveries.

The interest in the IGRB also stems from the consideration that the γ-ray band is a potential "golden channel" for the indirect detection of particle dark matter (DM). In fact, among the conventional astrophysical sources that contribute to the IGRB, there is the possibility that a characteristic signal from DM annihilation or decay may also be present. After its first detection and early attempts to shed light on the origin of the IGRB (see, e.g., Kraushaar et al. 1972; Fichtel et al. 1973; Mayer-Hasselwander et al. 1982; Padovani et al. 1993; Stecker & Salamon 1996; Sreekumar et al. 1998; Keshet et al. 2004; Strong et al. 2004), a significant step forward has recently been possible due to the *Fermi*-LAT which is resolving an ever growing number of sources (Nolan et al. 2012; Acero et al. 2015; Ackermann et al. 2015b), most of which have been identified as blazars, almost equally split into flat spectrum radio quasars (FSRQs) and BL Lacs sub-classes.

The properties of the resolved sources can be used to extrapolate their contribution to the IGRB (Ajello et al. 2012, 2014, 2015; Di Mauro et al. 2014b, 2014c). These population studies suggest that unresolved blazars account for only about 20% of the unresolved IGRB integrated above 100 MeV, while they can be the dominant component above few GeV. The remaining IGRB fraction is thought to be contributed by star-forming galaxies (SFGs) and misaligned active galactic nucleus (mAGN), two types of sources that can contribute 10%–50% each to the extragalactic γ-ray emission (Inoue 2011; Ackermann et al. 2012b; Di Mauro et al. 2014a). The contribution from additional potential sources like the millisecond pulsars located in our Galaxy at high Galactic latitudes turned out to be small (Siegal-Gaskins et al. 2011; Calore et al. 2014). The contribution from known astrophysical sources to the IGRB thus has significant uncertainties and

leaves room for an additional contribution by more exotic sources like DM.

Additional constraints on the origin of the IGRB can be obtained by analyzing the angular correlation properties of its fluctuations. Ackermann et al. (2012a, 2012b) and Cuoco et al. (2012) have confirmed the conclusions derived from the IGRB mean intensity and source populations studies: a blazar population that contributes, at energy below $\sim$10 GeV, about 20% of the unresolved IGRB can account for the whole measured angular power, thus providing an independent confirmation that the IGRB is not dominated by emission from blazars in the low-energy part of the spectrum. Constraints on the DM contribution have been derived in Ando & Komatsu (2013), Gómez-Vargas et al. (2014), and Fornasa et al. (2013).

The accuracy in the analysis of the IGRB and its fluctuations is limited by the presence of Galactic foregrounds and bright sources. If incorrectly subtracted, they can induce spurious contributions to both the mean IGRB intensity and its anisotropies. An effective way of dealing with this problem and to filter out contaminations is to cross-correlate the IGRB with maps of sources (observed in other wavelengths or by other means) that trace the same structures where the actual IGRB sources reside but do not correlate with Galactic foregrounds. Basically, all catalogs of extragalactic objects at any redshift satisfy these conditions. In the framework of the IGRB investigation, the cross-correlation strategy has been proposed in Cuoco et al. (2008) and Ando & Pavlidou (2009) and was recently revisited in Ando (2014) and Ando et al. (2014). The measurement was pioneered in Xia et al. (2011) using the first 21 months of *Fermi* data. In that case, no statistically significant signal was observed. The analysis has then recently been updated using 60 months *Fermi* maps (Xia et al. 2015). This time a significant (more than 3.5σ C.L.) cross-correlation signal has been detected. The signal is present on angular scales smaller than 1° in the cross-correlation between the diffuse γ-ray emission cleaned by the Galactic foregrounds and four types of large-scale structure (LSS) tracers: radio galaxies in the NRAO VLA Sky Survey (NVSS; Blake & Wall 2002), near-infrared-selected galaxies in the Two Micron All Sky Survey (2MASS; Jarrett et al. 2000), optically selected galaxies in the Sloan Digital Sky Survey (SDSS)-DR8 catalog (Aihara et al. 2011), and quasi-stellar objects (QSO) in the SDSS-DR6 catalogs (QSO-DR6; Richards et al. 2009). No significant correlation was observed with luminous red galaxies (LRGs) also from SDSS. The analysis further confirms that blazars provide a minor contribution, $<$20%, to the IGRB as found in the IGRB mean intensity and source populations studies, while a mixture of SFGs and mAGNs can in principle contribute to the majority of the IGRB.

A promising, possibly more effective in the context of DM, way to apply the cross-correlation technique is to use weak gravitational lensing maps (cosmic shear) instead of catalogs of LSS tracers (Camera et al. 2013, 2014; Fornengo & Regis 2014; Fornengo et al. 2014; Shirasaki et al. 2014). This alternative approach, originally proposed in Camera et al. (2013), has the advantage of directly probing the matter distribution, therefore avoiding the so-called "biasing" issue, i.e., the fact that the mapping between the spatial distribution of extragalactic sources and that of the underlying mass density field is ill-known and needs to be modeled. Cross-correlation of γ-rays with cosmic shear will become available in the next years with the release of cosmic shear maps from wide-area surveys such as, e.g., the Dark Energy Survey (DES; The Dark Energy Survey Collaboration 2005) and, in the next decade, by the satellite-based Euclid survey (Laureijs 2009). Finally, a similar technique, based on the cross-correlation of γ-rays with cosmic microwave background (CMB) lensing maps, has been recently adopted in Fornengo et al. (2014), where evidence of 3.2σ has been reported, providing a further direct evidence of the extragalactic origin of the IGRB and of a subdominant role of Galactic sources.

In this paper, we investigate the implications of the recent measurement of a cross-correlation between γ-rays and LSS tracers by Xia et al. (2015) for both the DM and the main astrophysical contributors to the IGRB. This work builds upon the results obtained by Regis et al. (2015), in which we concentrated on the low-redshift 2MASS catalog as a tracer of the LSS in the local universe, and we have assumed that DM-induced γ-rays provide the dominant source of cross-correlation for such a low-redshift observations. That approach has been motivated by the fact that the DM contribution to the cross-correlation is dominated by γ-ray emission at low redshift (see, e.g., Fornengo & Regis 2014 or Appendix A), which is where 2MASS galaxies mostly reside. In that analysis, we found that the observed cross-correlation signal can indeed be explained by a DM emission, while its contribution to the total mean intensity is significantly below the IGRB intensity measured by *Fermi*. This implies that the cross-correlation technique can be a powerful probe of the particle nature of DM, even when the DM contribution to the IGRB is subdominant, which is what we expect in a realistic scenario. In Regis et al. (2015), we found that the cross-correlation signal can be explained by a DM particle with mass in the tens to hundreds GeV range (depending on the γ-rays production channel) and, once the uncertainties in the DM distribution modeling is properly accounted for, a "thermal" value for the annihilation cross section ($\langle\sigma_a v\rangle = 3 \times 10^{-26}\,\mathrm{cm}^3\,\mathrm{s}^{-1}$), which is the most appealing case for a weakly interacting massive particle (WIMP) DM. From the same analysis, we have obtained upper bounds on the DM annihilation cross section and decay rate that turn out to be quite competitive with those obtained with different techniques, based either on local (Galactic halo, dwarf galaxies) or extragalactic γ-ray emission. We point out that those constraints are conservative precisely because the DM is assumed to be the only source of the γ-ray signal.

In this follow-up paper, we extend the study of Regis et al. (2015) to the inclusion of astrophysical γ-ray emitters, and to the whole set of LSS tracers catalogs. As will be discussed in the next sections, the redshift distributions of the γ-ray signal is a fingerprint that characterizes the contribution of different astrophysical sources and of the DM. For this reason, the possibility of using catalogs of objects whose distributions peak at different redshifts is an effective way to extract the information encoded in the γ-ray maps and remove degeneracies. To this aim, in addition to DM, here we account for contributions from blazars (of both BL Lac and FSRQs types), SFGs, and mAGNs. Consequently, we do not limit our cross-correlation study to the 2MASS catalog but consider NVSS, SDSS-DR6 QSO, LRGs, and SDSS-DR8 Main Galaxy samples as well. The approach will be similar to Xia et al. (2015), where, however, only astrophysical sources have been fitted to the observed correlations. Here, besides including DM

in the fit, we will use an improved description of the cross-correlation modeling between astrophysical sources and LSS tracers based on the halo occupation distribution (HOD) formalism. As for the DM, we shall use the halo model to trace its spatial distribution and predict its cross-correlation with LSS (see e.g., Cooray & Sheth 2002; Ando & Komatsu 2013; Fornengo & Regis 2014).

The paper is organized as follows. In Section 2, we present the theoretical estimate of the angular cross-correlation function (CCF) and angular power spectra (PS). Section 3 describes the statistical techniques employed in the determination of the parameters of the γ-ray emitters (DM and astrophysical sources) from the measured cross-correlation reported in Xia et al. (2015). Section 4 then shows our results, and finally Section 5 summarizes our conclusions. The technical aspects of our theoretical modeling are presented in a set of three Appendices. Appendix A introduces the modeling of the window functions of DM and astrophysical γ-ray sources and of catalogs of LSS tracers. Appendix B discusses the HOD of galaxies for the various catalogs. Appendix C describes the derivation of three-dimensional (3D) PS. These are the ingredients used in Section 2.

In this work, we assume a fiducial flat ΛCDM model with the cosmological parameters derived by the *Planck* Collaboration in Planck Collaboration et al. (2015): matter density parameter $\Omega_{\rm m} = 0.31$, baryon density parameter $\Omega_{\rm b}h^2 = 0.022$, reduced Hubble constant $h = 0.68$, rms matter fluctuations in a comoving sphere of 8 Mpc $\sigma_8 = 0.83$, and spectral index of primordial scalar perturbations $n_{\rm s} = 0.96$.

2. FORMALISM

To quantify the cross-correlation between γ-ray sources and the LSS tracers in the various catalogs, we consider both the two-point angular CCF and its Legendre transform, i.e., the cross angular power spectrum (CAPS). In the Limber approximation (Limber 1953; Kaiser 1992, 1998), the CAPS can be obtained by integrating the 3D PS of cross-correlation $P_{\gamma g}(k, z)$:

$$C_\ell^{(\gamma g)} = \int \frac{d\chi}{\chi^2} W_\gamma(\chi)\, W_g(\chi)\, P_{\gamma g}(k = \ell/\chi, \chi), \qquad (1)$$

where $\chi(z)$ denotes the radial comoving distance, $W(\chi)$ is the so-called window function that characterizes the distribution of objects and γ-ray emitters along the line of sight, k is the modulus of the wavenumber, and ℓ is the multipole. We relate the cosmological redshift z to the radial comoving distances χ through the differential relation, valid in a flat cosmology, $d\chi = c\, dz/H(z)$, where $H(z)$ is the expansion rate of the universe.

The indices γ and g denote γ-ray emitters and extragalactic objects in different catalogs, respectively. We consider five types of γ-ray sources: three different flavours of active galactic nuclei (AGNs; BL Lacs, FSQRs, mAGN), SFGs, and DM. We will consider both the case of annihilating and decaying DM particles. For the LSS tracers, we consider five different catalogs: quasars in SDSS-DR6, 2MASS galaxies, NVSS radio sources, SDSS-DR8 LRG, and SDSS-DR8 "main" galaxies.

Denoting the density fields of an LSS tracer with $f_g(\chi, r)$, and that of the gamma-ray emitter with $f_\gamma(\chi, r)$, where r indicates the position in comoving coordinates and χ labels time (given the one-to-one correspondence between time and distance), the cross-PS is defined as

$$\left\langle \hat{f}_\gamma(z, k) \hat{f}_g^*\left(z', k'\right) \right\rangle = (2\pi)^3 \delta^3\left(k + k'\right) P_{\gamma g}\left(k, z, z'\right), \qquad (2)$$

where $\hat{f}$ is the Fourier transform of $f(\chi(z), r)/\langle f(\chi(z))\rangle$, $\langle . \rangle$ indicates the average over the survey volume and the explicit dependence on z, and z' highlights the possibility that the two populations under study (γ-ray emitters and extragalactic LSS tracers) are located at two different redshifts. From the Limber approximation, one gets $\delta(z-z')$, so, in practice, only $P_{\gamma g}(k, z)$ is used. The modeling of the various PS used in our analysis is derived in Appendix C. Objects in the catalogs are described in terms of their HOD, which is discussed in Appendix B.

The window function $W_g(z)$ appearing in Equation (1) weights the contribution of objects at different redshifts to the cross-correlation signal. In the case of LSS tracers, it coincides with the redshift distribution of the objects, dN_g/dz. More precisely, $W_g(z) \equiv H(z)/c\, dN_g/dz$ such that $\int d\chi W_g(\chi) = 1$ for a redshift distribution dN_g/dz normalized to unity. The expressions of dN_g/dz for the different types of LSS tracers that we consider here are the same as in Xia et al. (2015; see also Appendix A.3).

For a γ-ray emitter the window function, $W_\gamma(\chi)$ can be defined in term of the γ-ray intensity integrated along the line of sight, $I_{f_\gamma}(n)$, as function of the direction in the sky n, which can be written as

$$I_{f_\gamma}(n) = \int d\chi\, \frac{f_\gamma(\chi, r)}{\left\langle f_\gamma(\chi)\right\rangle} W_\gamma(\chi) \qquad (3)$$

so that $\langle I_{f_\gamma}\rangle = \int d\chi\, W_\gamma(\chi)$. We will use a coordinate system centered on the observer so that $r = \chi\, n$. The expression of the density fields f_γ and window functions W_γ for the different classes of γ-ray sources are provided in Appendix A.

In the Appendices we also define our reference models for the astrophysical and DM γ-rays emitters, and for their cross-correlations with the LSS tracers. The mean intensity $I_\gamma = \langle I_{f_\gamma}\rangle$ as function of energy of the different γ-ray emitters for our reference models is shown in the left panel of Figure 1. The various curves in color indicate the contribution of each component, as indicated by the labels, while the black line indicates the sum of all astrophysical contributions. The predicted total energy spectrum matches the recent *Fermi*-LAT measurements (Ackermann et al. 2015a; solid dots with 1σ error bars). Similarly, as shown in the right panel of Figure 1, we also verified that our reference model matches the observed angular PS of the diffuse extragalactic gamma-ray background measured in the 1–2 GeV energy band by the *Fermi*-LAT (gray strip; Ackermann et al. 2012a). The different curves in color show the predicted angular PS of the various emitters that contribute to the total angular spectrum (solid black line). The model angular PS for the various gamma-ray emitters have been derived by using the PS of the source $P_\gamma\gamma$ instead of the cross-spectrum $P_{\gamma g}$, and $W_\gamma^2(\chi)$ instead of the product $W_g W_\gamma$ in Equation (1). With respect to the more accurate procedure used in Di Mauro et al. (2014b), here we use the simplifying assumption that all the sources of a given population have the same photon spectral index (see Appendix A).

In the next section we will fit the theoretical predictions to the measured cross-correlations and will estimate the free

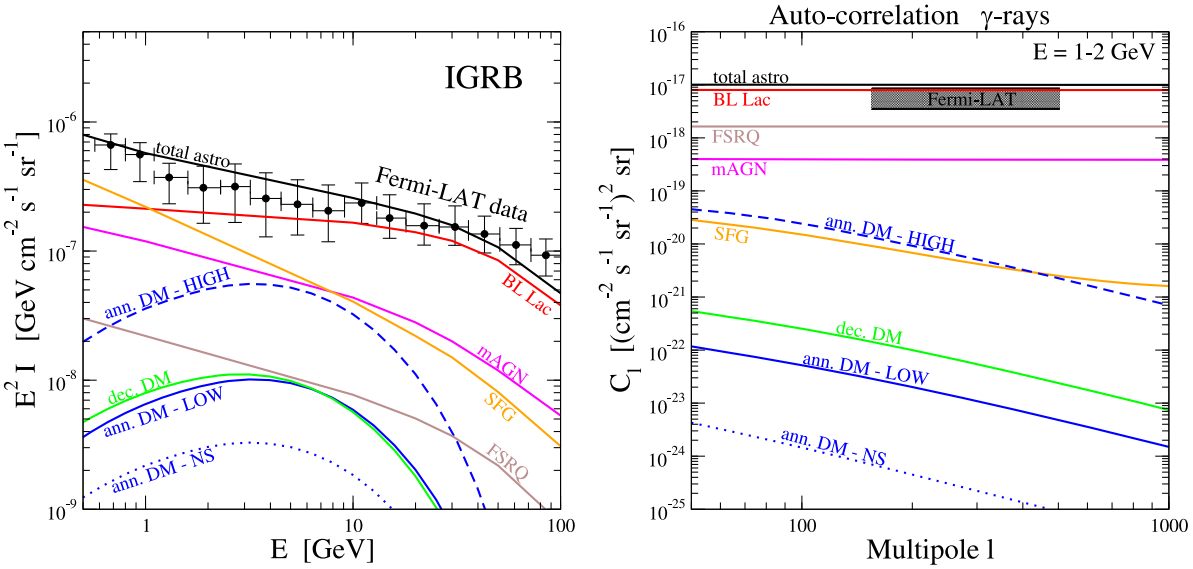

Figure 1. Average gamma-ray intensity I_γ as a function of photon energy (left) and auto-correlation APS $C_l^{(\gamma\gamma)}$ in the (1–2) GeV energy band (right) for the benchmark γ-ray models considered in this work. The black lines denote the total contribution arising from astrophysical sources (i.e., the sum of BL Lac, mAGN, FSRQ, and SFG emission). *Fermi*-LAT data are shown as black points (left, from Ackermann et al. 2015a, adding in quadrature systematic and statistical uncertainties) and a shaded region (right, from Ackermann et al. 2012a, including the measurements with and without foreground cleaning).

parameters of the models. For the astrophysical components, the results will be in the form of *deviations* from reference models, which we adopt from the literature as updated benchmarks. We will therefore allow variations only in their normalization, plus a correction term as specified in the next section.

A technical remark to take into account when comparing the model with the data is that the experimental CAPS determined from the data are *not* deconvolved from the effect of the point-spread function (PSF) of the instrument and the effect of map pixelization. To account for these effects, we thus convolve our model prediction in Equation (1) with the PSF and pixelization using the same procedure described in Xia et al. (2015). Formally, this is implemented defining the new quantity directly comparable with the data as $\tilde{C}_\ell^{(\gamma g)} = W_\ell^B\, C_\ell^{(\gamma g)}$ where the effective beam window function W_ℓ^B parameterizes the PSF and pixelization effects (see Xia et al. 2015 for more details).

Finally, in the following, we perform our analyses in terms of the cross-correlation function $\mathrm{CCF}^{(\gamma g)}(\theta)$ rather than the cross angular PS $C_\ell^{\gamma g}$. To obtain the CCF, we perform a Legendre transformation on our CAPS as follows:

$$\mathrm{CCF}^{(\gamma g)}(\theta) = \sum_\ell \frac{2\ell+1}{4\pi} \tilde{C}_\ell^{\gamma g} P_\ell[\cos(\theta)], \qquad (4)$$

where θ is the angular separation in the sky and P_ℓ are the Legendre polynomials.

3. STATISTICAL ANALYSIS

In order to assess the possible presence of a DM signal in the IGRB, and its robustness to the presence of astrophysical emitters, we perform a statistical analysis fitting the observed cross-correlation data of Xia et al. (2015) with a combination of both DM and astrophysical source models. Specifically, we define a χ^2 statistic from the data D, i.e., the observed CCF between the *Fermi* maps and the number of sources in catalogs (Xia et al. 2015), and M, i.e., the model CCF calculated for the different types of γ-ray emitters as introduced in the previous section and detailed in the appendices. The χ^2 is defined as

$$\chi^2 = \sum_{p=1}^{5}\sum_{n=1}^{3}\sum_{\theta_i\,\theta_j}\left(D_{\theta_i}^{(p,n)} - M_{\theta_i}^{(p,n)}(A)\right) \times \left[\mathcal{C}^{(p,n)}\right]^{-1}_{\theta_i\theta_j}\left(D_{\theta_j}^{(p,n)} - M_{\theta_j}^{(p,n)}(A)\right), \qquad (5)$$

where the index p runs over the 5 different catalogs of extragalactic sources (2MASS, NVSS, SDSS-DR6 QSO, SDSS-DR8 Main Sample Galaxies, and SDSS-DR8 LRG), the index n runs over 3 γ-ray energy ranges ($E > 0.5$ GeV, $E > 1$ GeV, and $E > 10$ GeV), whereas the indices θ_i and θ_j run over 10 angular bins logarithmically spaced between $\theta = 0.^\circ1$ and 100°. $\mathcal{C}^{(p,n)}$ is the covariance matrix that quantifies the errors on the CCFs in each angular bin and the covariances among different bins, and A denotes the vector of free parameters which the CCF model M depends upon (specified below). Both the covariance matrix $\mathcal{C}^{(p,n)}$ and the measured CCFs $D_{\theta_i}^{(p,n)}$ are taken from Xia et al. (2015). In Equation (5), the total χ^2 is obtained by adding up the individual χ^2 computed in three overlapping energy bands. There is thus in principle, a statistical dependence among the different energy bands that should be accounted for. Nonetheless, such dependence is expected to be small since photon counts are heavily dominated by events near the lower end of each energy interval because of the steep IGRB energy spectrum $\propto E^{-2.3}$ (Ackermann et al. 2015a). For this reason, we will treat the CCFs estimated in the three energy intervals as statistically independent in the χ^2 analysis.

For any given catalog of LSS tracers, energy band, and angular bin (i.e., for a given choice of p, n, and θ_i), the theoretical CCF $M_{\theta_i}^{(p,n)}$ can be expressed as a sum of different

contributions:

$$M_{\theta_i}^{(p,n)} = \sum_{\alpha=1}^{5} A_\alpha c_\alpha^{(p,n)}(\theta_i) + A_{1h}^{(p)} c_{1h}^{(n)}(\theta_i). \quad (6)$$

The sum runs over the five different γ-ray emitters: BL Lacs, FSRQs, SFGs, mAGNs, and DM. The terms $c_\alpha^{(p,n)}(\theta_i)$ denote the benchmark theoretical model CCFs described in the Appendix and A_α is a free normalization parameter that quantifies the individual contribution to the observed cross-correlation. Values $A_\alpha = 1$ thus denote models equal to our benchmarks, while values $A_\alpha \neq 1$ would correspond to deviations from the benchmarks.

Besides the normalization of each component, we have introduced in the fit also a further free parameter, A_{1h}, which we call the one-*halo correction term*. This term is introduced as a correction for possible inaccuracies in the modeling of the one-halo contribution of the PS (and thus mainly to the small-scale cross-correlation signal) of the γ-ray sources (hence its name), as discussed after Equation (28) in Appendix C. For simplicity, we model it as a constant term added in the CAPS, which is a good approximation of the one-halo term itself for astrophysical components, except at very high multipoles $\ell > 1000$, which we do not considered in our analysis. In real space, and taking into account the modulation introduced by the PSF of the instrument, the one-*halo correction term* $M_{1h}^{(p,n)}(\theta_i)$ explicitly reads

$$M_{1h}^{(p,n)}(\theta_i) = A_{1h}^{(p,n)} \sum_\ell \frac{2\ell+1}{4\pi} W_\ell^{B_n} P_\ell\left[\cos(\theta_i)\right], \quad (7)$$

where $W_\ell^{B_n}$ is the (energy-dependent) window function of the PSF, also introduced in the previous section. For definiteness, we have assumed that $M_{1h}^{(p,n)}$ has the same energy dependence as the IGRB spectrum $\propto E^{-2.3}$. With this assumption, we can separate the energy dependence from that on the source catalog $A_{1h}^{(p,n)} = A_{1h}^p f_n$ where $f_n = 2.46,\ 1,\ 0.05$ for $E_n > 0.5,\ 1,\ 10$ GeV (we take $E = 1$ GeV as the normalization energy). In this way, combining Equations (6) and (7), we have: $c_{1h}^{(n)} = f_n \sum_\ell \frac{2\ell+1}{4\pi} W_\ell^{B_n} P_\ell$. Note that, in principle, each candidate γ-ray emitter has its own *one-halo correction term* for each catalog and energy band. However, they are degenerate and only their sum can be constrained. We have thus grouped them together so that in Equation (6) the reported *one-halo correction term* actually represents the sum of the *one-halo correction terms* from all the components, for a given catalog and energy band.

All five values A_{1h}^p are treated as free parameters in the analysis. Note that they can be either positive or negative since we intend them as possible corrections to our benchmarks and the natural expectation would thus be $A_{1h}^p = 0$ if the benchmarks are correct. The whole set of A_α and A_{1h}^p coefficients (plus the additional parameter represented by the DM mass, upon which the DM signal depends) defines the parameter vector A of Equation (5), which represents the full set of parameters over which our analysis is performed.

For what concerns the particle DM contribution, we consider both the case where γ-rays are produced through DM particle annihilation and the case of DM decay. The DM mass is varied from 10 GeV to 5 TeV and we will show the results for a DM which dominantly annihilates/decays into one of the following γ-ray production channels: $b\bar{b}$, $\mu^+\mu^-$, $\tau^+\tau^-$, and W^+W^-. For annihilating DM, the signal strongly depends on the clustering at small scales and, in particular, on the amount of substructures. As discussed in Appendix A, results will be shown for three DM substructure models: HIGH, LOW, and NS. This will bracket the uncertainty on the reconstructed DM parameters arising from DM structure modeling. The HIGH scenario provides a more optimistic case with the largest boosting factor for the γ-ray annihilation flux. The NS scheme, where DM substructures are absent, provides a lower limit to to the annihilation signal and therefore represents the most conservative scenario. Finally, the LOW scheme represents an intermediate case which can be (currently) considered as the most realistic one and that we regard as our reference model. Each one of these three scenarios predicts a different CCF, $c_\alpha^{(p,n)}(\theta_i)$ with $\alpha = \mathrm{DM}$ in Equation (6). Since the intensity of the DM signal is proportional to the DM annihilation cross section $\langle\sigma_a v\rangle$ (or DM decay rate, Γ_d), we normalize our calculations to the reference values $\langle\sigma_a v\rangle_0 = 3 \cdot 10^{-26}\,\mathrm{cm^3\,s^{-1}}$, i.e., the so-called "thermal value" which corresponds to a DM particle thermally produced in the early universe which alone would account for the observed DM relic abundance. For decaying DM, we normalize the models to a decay rate of $\Gamma_{\mathrm{d},0} = 1.67 \cdot 10^{-28}\,\mathrm{s^{-1}}$, which is the decay rate which would produce a DM signal equal to the one of an annihilating DM with thermal cross section in the LOW substructure scheme (for DM masses around 100 GeV). The parameter A_α for $\alpha = \mathrm{DM}$ can thus be seen as the annihilation or decay rate in units of $\langle\sigma_a v\rangle_0$ or $\Gamma_{\mathrm{d},0}$, respectively.

In summary, the global fit will be performed in a one-dimensional (1D) parameter space, with the parameter vector given by $A = (A_\mathrm{DM}, m_\mathrm{DM}, A_\mathrm{BLLac}, A_\mathrm{mAGN}, A_\mathrm{SFG}, A_\mathrm{FSRQ}, A_{1h}^{k=1,2,3,4,5})$. All the parameters in the fit are linear, except m_DM which enters non-linearly in the fit through $c_\mathrm{DM}^{(k,n)}(\theta_i)$. Beside the above fit, we will also consider different configurations, namely different parameter vectors A, to cross-check the robustness of the results. In particular, we will consider the case where the A_{1h}^k are set equal to zero. These additional analyses will be described in more detail in the next section.

In order to efficiently scan the multi-parameter space, we adopt the Markov Chain Monte Carlo (MCMC) strategy publicly available in the *cosmomc* package (Lewis & Bridle 2002). We will use linear priors limited to positive values for the normalization of the astrophysical components A_BLLac, A_mAGN, A_SFG, A_FSRQ, although we will also check log priors. For the A_{1h} parameters we allow for linear priors with negative values since the *one-halo correction term* can either correct for the overestimation or under-estimation of the small-scale cross-correlation. Finally, we will use a logarithmic prior for A_DM and m_DM since, theoretically, the possible values of the DM mass and signal normalization can span several orders of magnitude.

Note that in our χ^2 analysis we consider only the cross-correlation signal and ignore the intensity and the auto-correlation of the IGRB. These additional observational inputs will be used to perform an independent a posteriori check on the validity of our results. While the total intensity I_γ and the γ-rays auto-correlation $C_l^{(\gamma\gamma)}$ calculated from the derived best-fit configurations must not exceed the measured values (this will be a sanity check), if they fall short of accounting for the data this might indicate either that the measured IGRB contains an unaccounted contribution which does not correlate with

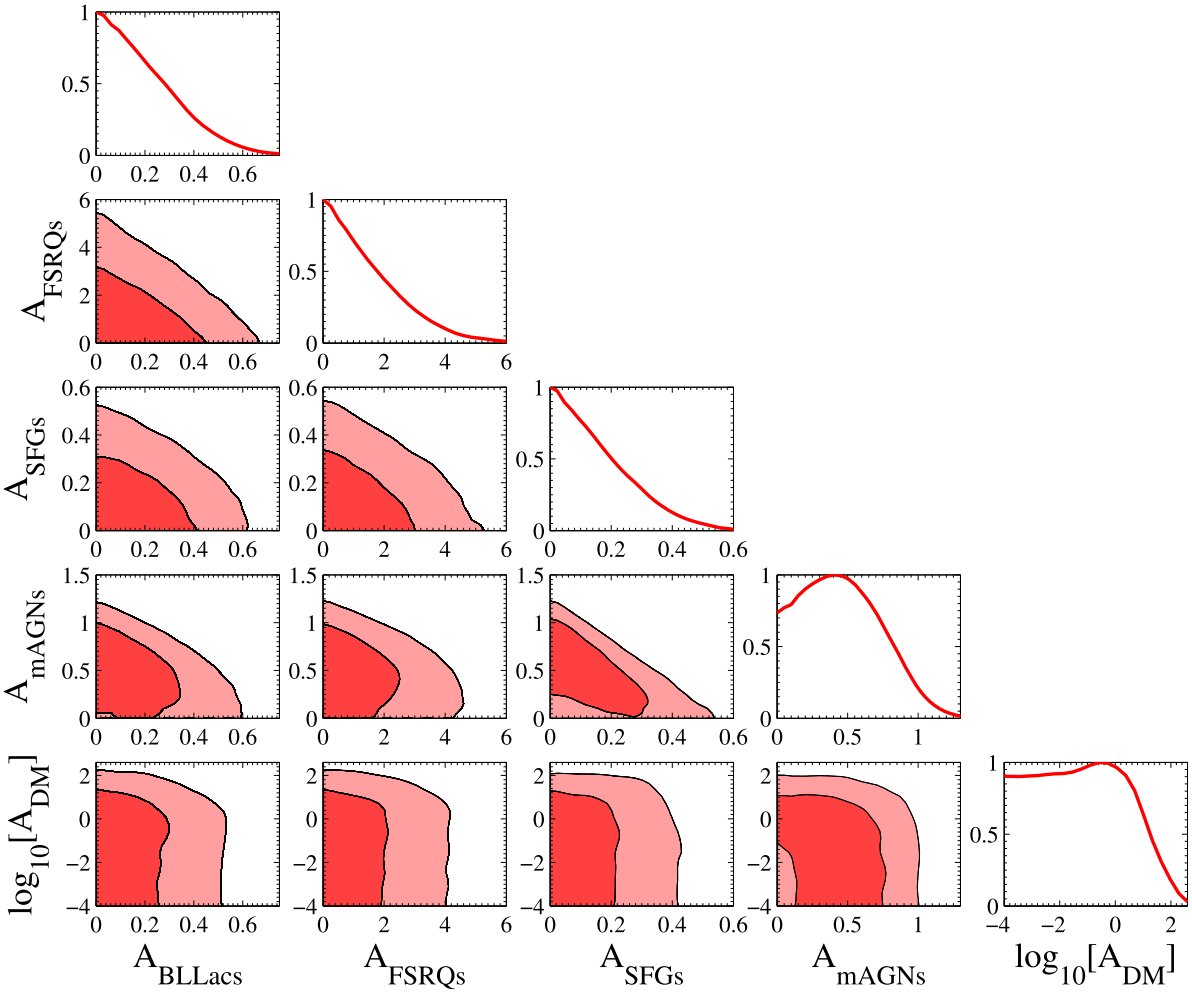

Figure 2. Triangle plot of the parameters posterior distributions, for our reference fit setup, for the LOW DM substructure scheme and for a DM particle annihilating into $b\bar{b}$. The darker (innermost) and the lighter (outermost) areas denote the 1σ and 2σ credible regions, respectively, for each combination of parameters considered in the analysis. The plots along the diagonal show the marginalized 1D posterior distributions for each parameter. Note that, for clarity, only the 5×5 sub-triangle plot with the A_α parameters is shown, instead of the full 11×11 full triangle plot, which includes also the dark matter mass $m_{\rm DM}$ and the one-halo correction $A_{1h}^{(k)}$ amplitudes.

extragalactic tracers (possibly of Galactic origin) or that the modeling of the known components is imperfect/incomplete. We will discuss more in detail these aspects in Section 4.1 and in the conclusions.

4. RESULTS AND DISCUSSION

The triangle plot shown in Figure 2 summarizes the results of our analysis for a benchmark annihilating DM case with $b\bar{b}$ final state and LOW substructure scheme. The plot shows the posterior marginal distributions of the normalization parameters A_α. The two-dimensional (2D) plots refer to the 1σ and 2σ credible regions for each pair of parameters, while the diagonal shows the 1D posterior distribution for each parameter. The parameter space is 11-dimensional, but for clarity we show only a part of the full triangle plot (without including here the parameters A_{1h}^k and $m_{\rm DM}$). The 2D posterior of ($A_{\rm DM}$, $m_{\rm DM}$) is shown separately in the left panel of Figure 3. The posterior probability for $m_{\rm DM}$ is instead displayed in the right panel of Figure 3, while the 1D posteriors for the A_{1h}^k parameters are shown in Figure 4. Finally, Figure 5 shows the best-fit results compared with the measured cross-correlation functions.

A noticeable result from Figure 2 is the fact that all the A_α posteriors seem to peak at $A_\alpha = 0$ or close to it, except (but with a low significance) for the DM and mAGN contributions. This does not necessarily imply that the best fit is found when the contributions from all components is zero. Instead, it is an indication that strong degeneracies are present. A 2D analogy is given by a case with only two parameters related by a simple relation $A_1 + A_2 = \text{const}$. While the degeneracy would be clearly seen in the 2D posterior, both the 1D A_1 and A_2 posteriors peak at zero, although A_1 and A_2 are never both zero at the same time. This is precisely the results we find here, although the high dimensionality of our parameter space prevents us from clearly tracing the parameter degeneracy even in the 2D posteriors plots.

The degeneracy of the different astrophysical components can be traced to the behavior of their respective window functions $W(z)$, which possess a relatively similar evolution as a function of redshift, and to a similar behavior of their cross-correlation 3D PS. As can be seen in Figure 13 in Appendix A, apart from the DM case for which the γ-ray emission is concentrated at low redshift with a fast decrease for increasing distances, astrophysical sources possess a relatively broad kernel. Figures 14 and 16 instead show some examples of 3D

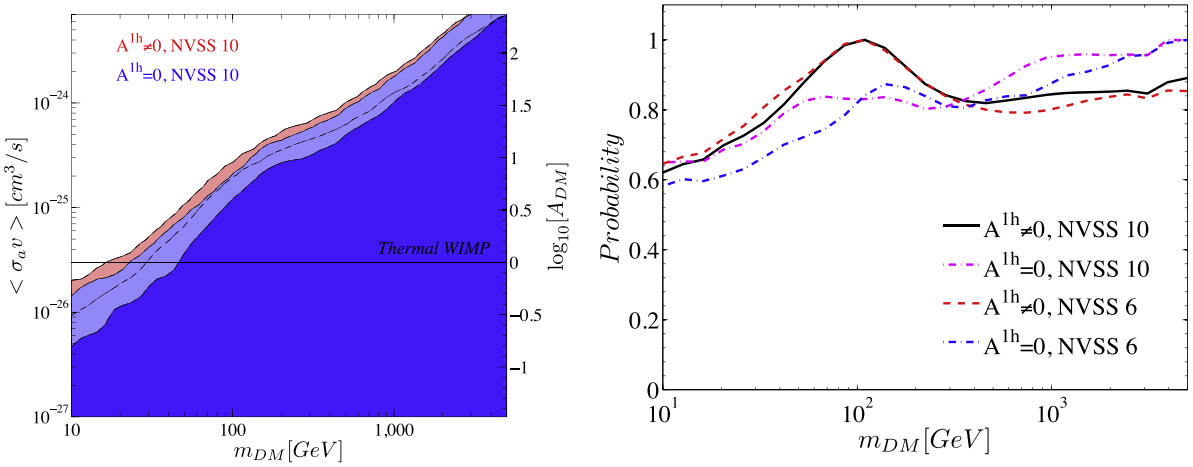

Figure 3. Left: 1σ and 2σ allowed credible regions for the annihilation rate $\langle\sigma_a v\rangle$ vs. the DM mass $m_{\rm DM}$ in the NVSS-10 $A^k_{1h} = 0$ (blue) and NVSS-10 $A^k_{1h} \neq 0$ (red) fit setups. A DM particle annihilating into $b\bar{b}$ and the LOW substructure scheme are assumed. The lower 1σ and 2σ contours of both cases extend down to $\langle\sigma_a v\rangle = 0$ (therefore providing only upper limits on the annihilation rate). Right: marginalized 1D posterior probability for the DM mass for the same DM annihilation channel ($b\bar{b}$) and substructure scheme (LOW) as in the left panel. The four lines refer to the four different fit setups described in the text, as labeled.

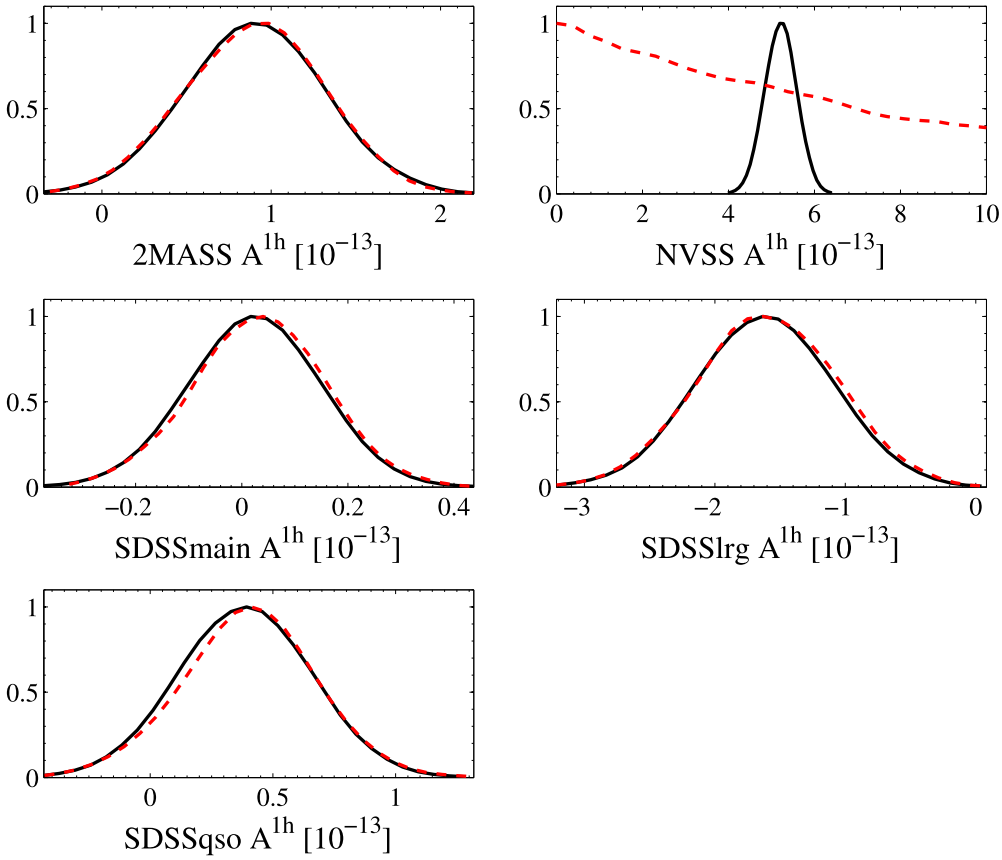

Figure 4. Marginalized 1D posterior probabilities for the one-halo correction terms A^k_{1h}, for the NVSS-10, $A^k_{1h} \neq 0$ (black solid) and NVSS-6, $A^k_{1h} \neq 0$ (red dashed) fits. They are in units of $10^{-13}\,{\rm cm}^{-2}\,{\rm s}^{-1}$.

cross-spectra between LSS tracers and the various astrophysical sources considered here or DM: we note that, for a given LSS tracer (e.g., 2MASS in Figure 14), the behaviors are quite similar for all astrophysical sources (while, instead, differences can be appreciated for the DM case). These facts, together with the relatively large error bars, makes astrophysical component separation currently difficult. On the other hand, given the somewhat different 3D cross-spectra, perspective to separate the DM component are perhaps brighter.

An exception in this line of reasoning are mAGNs and SFGs, which exhibit a significant degree of degeneracy with DM in the 2D posterior contours. The main features of the DM signal is that it peaks at low redshift and that it is mostly contributed by massive halos. To mimic such a signal, an astrophysical source must then preferentially be hosted in large halos at low z. Both SFGs and mAGNs meet the redshift requirement while the blazars do not, since their window peaks at higher z. However, only mAGNs are believed to be hosted in large

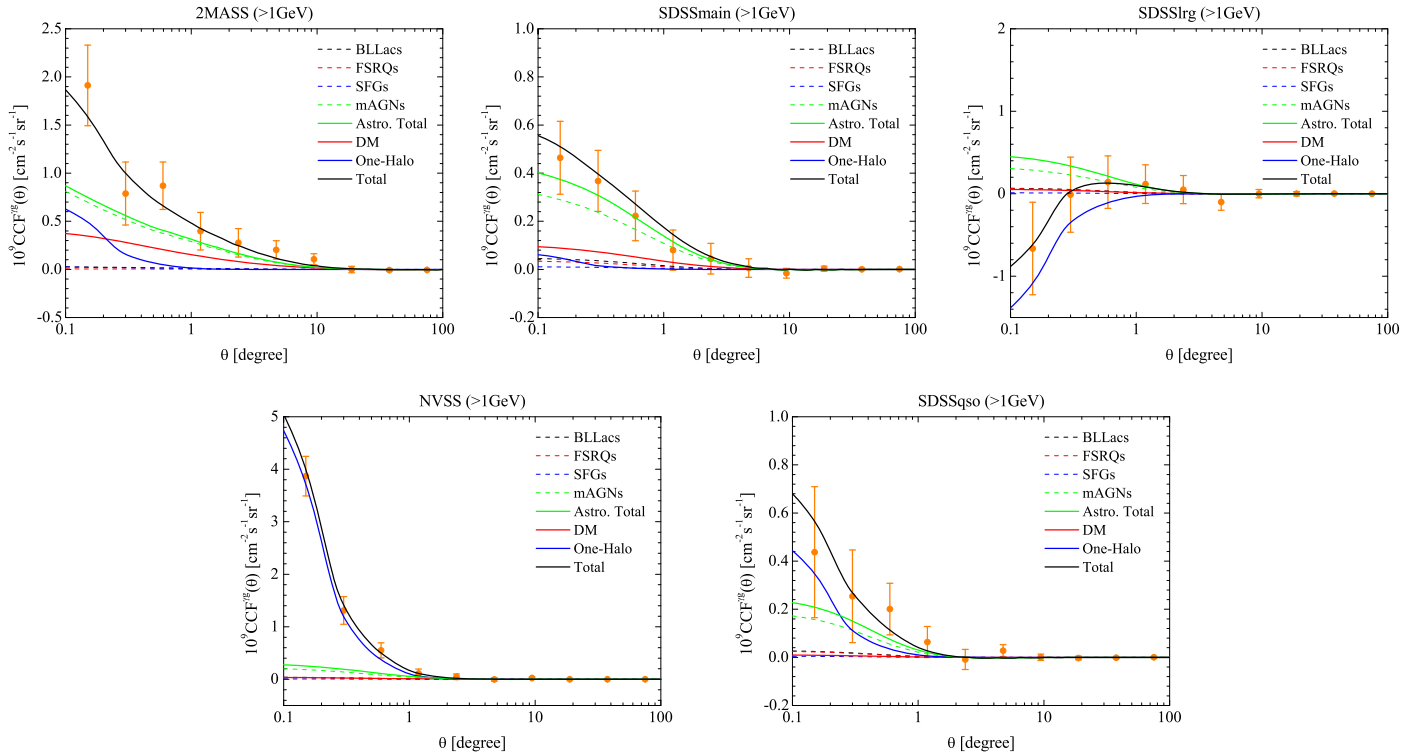

Figure 5. Measured cross-correlation function (CCF; Xia et al. 2015) for $E > 1$ GeV, as a function of the angular separation θ in the sky, compared to the best-fit models of this analysis. The contribution to the CCF from the different astrophysical γ-ray emitters (BL Lac, mAGN, SFG, FSRQ) are shown by dashed colored lines, while their sum ("Astro Total") and the DM contribution are indicated by solid green and red lines, respectively. The *one-halo correction term* is shown as a solid blue line. The total contribution to the CCF is given by the black solid line. The analogous plots for $E > 0.5$ GeV and $E > 10$ GeV are shown n Appendix D.

halos, while SFGs typically populate galaxy-size halos. Objects in large halos at low redshifts are expected to have a large bias and, more importantly, their correlation properties at the megaparsec scale is dominated by a large one-halo term. This introduces a characteristic feature in the cross-PS that differentiates mAGNs from SFGs, making their contribution more similar to the DM one at ∼megaparsec scales (see the left panel of Figure 15). At the lowest redshift considered (namely, in the cross correlation with 2MASS), the megaparsec scale corresponds to a sub-degree scale in the CCF. Nonetheless, given the present still large error bars, the above feature is only weakly constrained and thus a further degeneracy of both components with SFGs still remains on top of the mAGN-DM main degeneracy. Further investigation of this issue is reported later below. Instead, further differences between the mAGNs and and the DM cases are expected at smaller angles which, unfortunately, cannot be investigated given the size of the *Fermi*-LAT PSF.

Difficulties in modeling the one-halo term in the HOD framework described in Appendix B propagates into uncertainties in predicting the cross-power at small angles. To account for this potential source of systematic errors, we introduced in Equation (7) the one-halo correction terms $m_{1h}^{(k,n)}$. The 1D marginalized posteriors of the associated extra five parameters A_{1h}^k are shown in Figure 4 as black solid curves. The various data sets are consistent with the case $A_{1h}^k = 0$ with different confidence levels, except NVSS. In this case, we find a strong and statistically significant deviation from zero. This can also be appreciated in the fit to the observed CCF in Figure 5 where the presence of a prominent one-halo correction term is required to fit the data at small angles. There is a likely explanation for this additional contribution: the presence in the NVSS catalog of γ-ray point sources (i.e., AGN) that are just below the *Fermi* detection threshold. These sources would add their auto-correlation signal at zero-lad that, because of the PSF, spreads out to $\sim 1^\circ$ scale. This effect requires some fine tuning of the parameters defining the one-halo term in Equation (28) which the benchmark model fails to catch, thus requiring a large correction term. The effect is also discussed in Xia et al. (2015), to which we refer the reader for further discussion. The relevance of this term in the fit to NVSS data is expected to affect our constraints of the DM properties. To investigate this issue, we use three further fitting procedures in addition to the one adopted so far. The four fitting procedures are as follows.

1. *NVSS-10*, $A_{1h}^k \neq 0$. All the 10 NVSS data points are fitted and the *one-halo correction terms* are free parameter of the fit. This is the standard fitting procedure used to obtain the results shown in Figure 2.
2. *NVSS-10*, $A_{1h}^k = 0$. All the 10 NVSS data points are fitted and all the o*ne-halo correction terms* are set equal to zero.
3. *NVSS-6*, $A_{1h}^k \neq 0$. The first four NVSS data points at small angles are excluded from the fit. The *one-halo correction terms* are used as free parameters in the fit.
4. *NVSS-6*, $A_{1h}^k = 0$. The first four NVSS data points are excluded from the fit. All *one-halo correction terms* are set equal to zero.

Figure 4 shows the A_{1h}^k posteriors for the NVSS-10, $A_{1h}^k \neq 0$ (black solid curves) and the NVSS-6, $A_{1h}^k \neq 0$ (red dashed

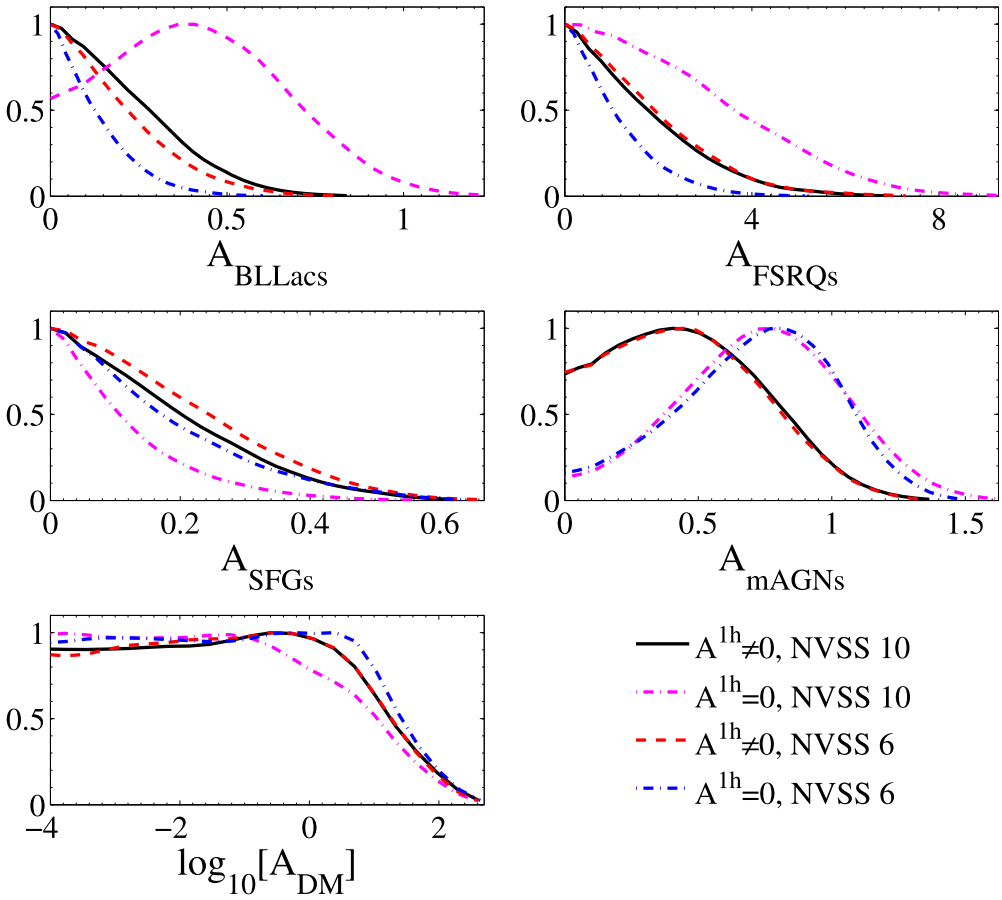

Figure 6. Marginalized 1D posterior probabilities for the A_α terms.

curves) cases. It can be seen that there are no significant differences between the two fitting schemes, except for the NVSS case in which A_{1h}^k becomes obviously unconstrained when the first four data points, where the fit is guaranteed by the *one-halo correction term*, are ignored. Figure 6 quantifies the impact of the four fitting schemes on the posterior probabilities of all A_α parameters. The plots show that the fitting procedure does have an impact on some A_α parameter. In particular, the results obtained with the NVSS-10, $A_{1h}^k = 0$ fit deviates from the others in most of the cases. However, this is also the scheme that provides the worst fit to the various data sets, as illustrated by the comparatively larger χ^2 values listed in Table 1, so that the results from this case are likely somewhat biased. Instead, all the three remaining schemes provide reasonably good fits to the different data sets. The NVSS-6, $A_{1h}^k = 0$ case provides a slightly worse fit to the data, particularly to the LRG sample, than the other schemes. It is interesting to note that this fitting scheme favors a non-zero mAGN component (see the $A_{\rm mAGN}$ panel in Figure 4) which is absorbed by the *one-halo correction term* when a fitting scheme with $A_{1h}^k \neq 0$ is adopted. This indicates that a degeneracy between the A_{1h}^k and the $A_{\rm mAGN}$ parameter is present. We note that in all three cases the χ^2 is lower than total number of degrees of freedom. This is partly due to some unaccounted correlation between the three energy bins and between the different catalogs, and partly to the fact that the error bars are probably slightly overestimated. Indeed, it is known that the algorithm implemented in the PolSpice software which is used in Xia et al. (2015) is not a minimum variance estimator of the error bars, i.e., it does not provide the smallest error possible (Efstathiou 2004).

Let us now discuss in more details the implications for the DM component. From the CCF plot in Figure 5 we see that DM provides a significant contribution to the fit. Yet, the posterior probability of $A_{\rm DM}$ in the bottom right panel of Figure 2 does not provide a clear indication for a DM component. As discussed above, this is an indication that a DM signal may indeed be there but is degenerate with some other component, in particular the mAGN one. In practice, the present data sets and our cross-correlation analysis cannot distinguish between the case of a large DM contribution with subdominant mAGN signal and that of a mAGN signal that dominates over the DM contribution. In fact, the situation is further complicated by the aforementioned degeneracy between mAGN and the 1-halo-correction terms. Before discussing the degeneracy issue more in detail, it is worth pointing out that (i) our results are robust to the choice of the fitting strategy, as shown in the right panel of Figure 3 and in the bottom panel of Figure 6, and that (ii) despite the DM versus mAGN degeneracy we are able to set constraints on the annihilation cross section, as shown in the left panel of Figure 3, able to exclude the thermal value at 2σ for DM masses up few tens of GeV (in the LOW substructure scheme) that, again, are robust against the adopted fitting scheme. We also verified the robustness of the DM constraints with respect to the choice of the priors for the astrophysical components. Specifically, we considered the case of log-flat priors instead of a linear-flat ones, and we found that the posteriors of the DM parameters

Table 1
Best-fit $\chi^2_{\rm bf}$ for the Four Analyses Described in the Text, Broken Down into the Contributions from the Three Energy Bands (E_{05}, E_1 and E_{10} Stand for $E > 0.5$, 1, 10 GeV, Respectively) and the Five Catalogs Used

$\chi^2_{\rm bf}$	2MASS			SDSS-MG			SDSS-LRG			SDSS-QSO			NVSS			TOTAL				
	E_{05}	E_1	E_{10}	E_{05}	E_1	E_{10}	E_{05}	E_1	E_{10}	E_{05}	E_1	E_{10}	E_{05}	E_1	E_{10}	E_{05}	E_1	E_{10}	All E	$N_{\rm dof}$
NVSS-10 $A^k_{1h} \neq 0$	6.5	8.5	2.5	4.0	2.5	6.3	2.4	2.1	3.0	16.8	4.2	6.9	3.8	3.7	6.6	33.5	21.1	25.3	79.9	$150-11$
NVSS-10 $A^k_{1h} = 0$	6.4	12.5	2.7	13.5	6.4	8.9	10.1	9.5	4.0	13.9	3.8	4.9	68.1	84.6	56.1	112.1	116.9	76.6	305.6	$150-6$
NVSS-6 $A^k_{1h} \neq 0$	6.4	8.8	2.3	3.3	2.4	6.8	2.3	2.1	2.9	17.4	4.4	7.1	1.5	2.1	2.6	31.0	19.8	21.7	72.5	$138-11$
NVSS-6 $A^k_{1h} = 0$	6.2	11.3	2.3	4.8	2.6	6.8	6.4	6.3	2.9	19.0	4.7	6.2	1.5	2.0	2.5	38.0	27.0	20.8	85.8	$138-6$

Note. The number of degrees of freedom, $N_{\rm dof}$, is expressed as the total number of data points minus the number of free parameters in the fit.

are unaffected. Some small variations are present in the constraints of the astrophysical parameters, which is expected since at the moment the significance of the measurement is still not very high, and in this regime some prior dependence is typically still present.

One thing to notice about the DM versus mAGN degeneracy is that few mAGNs have been detected in γ-rays so far. As a consequence their model contribution to the IGRB and its anisotropies is rather uncertain. One key quantity is the relation between the γ-ray luminosity of these objects, $\mathcal{L}$ and the mass of their host halo M. Varying this relation within its uncertainty range, which is rather large (see e.g., Camera et al. 2014), modifies the predicted cross-correlation signal. Figure 15 illustrates this point. In the right panel we show the cross-PS mAGN-2MASS galaxies (solid line) and how it changes when the $M(\mathcal{L})$ relation is varied within its uncertainty band (dashed curves). Considering halo masses in the lower bound of the uncertainty strip significantly decreases the amplitude of the 1-halo term and reduces the amplitude of the PS on Mpc scales. As a result the PS contributed by mAGNs will be very similar to that contributed by SFG, as shown in the left panel of Figure 15, and since their window functions are also very similar (see Figure 13), their contributions to the cross-power become fully degenerate.

We are therefore entitled to consider a scenario in which, due to this degeneracy, we set the mAGN contribution equal to zero and assume that it is absorbed by the SFG one. To explore this situation we consider four additional fitting schemes. In all of them we ignore the first data points of the NVSS dataset (i.e., we use the NVSS-6 scheme) and set $A_{\rm mAGN} = 0$. The four schemes are obtained from all possible combination of $A_{\rm DM}$ and A_{1h}^k that are either set equal to zero or let free to vary. The four combinations are explicitly shown in the first column of Table 2 in which we summarize the results of the χ^2 analysis.

The inclusion of the one-halo correction terms improves the fit appreciably, although the improvement is mainly driven by the LRG and QSO data sets. The inclusion of DM with two extra-parameters also improves the fit decreasing the best-fit χ^2 by 4.3 and 5.8 for the fits with and without one-halo correction terms, respectively, with improvement mainly coming from a better fit to the 2MASS data. No scheme provides a good fit to the CCF with the QSO for $E > 500$ MeV. This is possibly an indication of an imperfect modeling of the energy spectrum in the QSO correlation.

Figure 7 shows the triangle plot for the case $A_{\rm DM} \neq 0$ and $A_{1h}^k = 0$. When the mAGN contribution is suppressed ($A_{\rm mAGN} = 0$), a non-vanishing DM component provides quite a good fit, with about a 2σ deviation from zero. Furthermore, the best-fit χ^2 values in Table 2 are very similar to those in Table 1 in which the mAGN component was included in the model (71.6 versus 72.5 and 89.5 versus 85.8 for the case with and without one-halo correction terms, respectively), a fact that corroborates the evidence for a degeneracy between DM and mAGNs. Figure 8 illustrates the robustness of these results to the inclusion of the one-halo correction term, $A_{1h}^k \neq 0$, for two different final annihilation states: $b\bar{b}$ (left set of plots) and and $\tau^+\tau^-$ (right plots). In all cases, the best fits preference is for the presence of a DM component, even when the extra degree of freedom A_{1h}^k is included. Furthermore, these plots reveal a degeneracy between $A_{\rm DM}$ and $m_{\rm DM}$, which is to be expected since, as can be seen in Equation (10), the WIMP signal approximately scales with $A_{\rm DM}/m_{\rm DM}$. Indeed, W_{δ^2} contains a factor $\langle\sigma_a v\rangle/m_{\rm DM}^2$ plus an integral over the energy which introduces a contribution roughly proportional to $m_{\rm DM}$ (being the spectrum integrated up its end-point, which is $m_{\rm DM}$). Inspection of Figure 7 also shows more clearly the degeneracy between DM and the SFG components, left from the mAGN-DM-SFG degeneracy after removing the mAGN component. One consequence of this is that performing a fit excluding either the SFG or the mAGN component would enhance the strength of the DM signal, without affecting appreciably the value of the best-fit χ^2.

In conclusion, our analysis indicates that a significant DM contribution to cross-correlation is entirely plausible. However, the degeneracy with other astrophysical sources, namely mAGNs and SFGs, largely originating from the current observational uncertainties, prevents us from drawing a definitive conclusion. Future analyses with increased γ-ray statistics and improved angular resolution in which the cross correlation is extended to other catalogs of extragalactic objects will help to break the present degeneracies and to pinpoint the correct scenario.

As a final remark, we also mention that, as a cross-check, we have performed the analysis employing the astrophysical models adopted in Xia et al. (2015). The constraints on the γ-ray astrophysical contributions are different, which is expected given the different modeling. Regarding DM, using the NVSS-6, $A_{\rm mAGN} = 0$, $A_{1h}^k = 0$ fit configuration, which is the closest to the one used in Xia et al. (2015), we compare in Figure 9 the DM posteriors from three different fits using three different SFG models: the one adopted in this work (black solid curve), the SFG1 model from Xia et al. (2015; red dashed curve), and a modified version of SFG1 (blue dotted–dashed curve) with redshift-dependent bias equal to the the bias of the present model (while the original SFG1 model has bias equal to 1 for all z). The SFG2 model of Xia et al. (2015) is very similar to present SFG model and is not considered. The plot indeed shows that the DM results are not significantly dependent from the SFG model adopted.

With no unambiguous indication for a DM components, we can nevertheless set constraint on the properties of the DM candidates. To this purpose, we perform, for any given mass of the DM particle candidate, an individual 10 parameter fit and set the 95% bound on $\langle\sigma_a v\rangle$ from the posterior distribution. The results for the annihilating DM are summarized in Figure 10. In the left panel, we focus on the $b\bar{b}$ annihilation channel. The solid line with different colors refer to constraints obtained from each of the three energy band separately ($E > 0.5$, 1, 10 GeV) as well as the ones obtained by their combination (red line). All the results refer to the LOW substructures model and are obtained with the reference NVSS-10 $A_{1h}^k \neq 0$ fitting scheme. The upper and lower dotted–dashed curves show how the bounds change in the the NS and HIGH substructure model, respectively.

In the right panel, we compare the results of different final annihilation channels ($\mu^+\mu^-$, $\tau^+\tau^-$, and W^+W^-) to the original $b\bar{b}$ case (red curve) shown in the left plot for the LOW substructures scenario and combining all energy bands. All the results refer to the benchmark NVSS-10 $A_{1h}^k \neq 0$ case, but the other fitting schemes provide nearly indistinguishable constraints. The black curve is taken from Regis et al. (2015) and refers to the case in which we assumed that all the 2MASS γ-ray correlation is produced by DM, with no astrophysical contribution. As expected, including the astrophysical sources makes the constraints stronger by

Table 2

Best Fit $\chi^2_{\rm bf}$ for the Four NVSS-6, $A_{\rm mAGN} = 0$ Setup, Broken Down into the Contributions from the Three Energy Bands (E_{05}, E_1, and E_{10} Stand for $E > 0.5$, 1, 10 GeV, Respectively) and the Five Catalogs Used

$\chi^2_{\rm bf}$	2MASS			SDSS-MG			SDSS-LRG			SDSS-QSO			NVSS			TOTAL				
	E_{05}	E_1	E_{10}	E_{05}	E_1	E_{10}	E_{05}	E_1	E_{10}	E_{05}	E_1	E_{10}	E_{05}	E_1	E_{10}	E_{05}	E_1	E_{10}	All E	$N_{\rm dof}$
$A^k_{lh} \neq 0 A_{\rm DM} \neq 0$	7.0	8.0	2.3	3.1	2.4	6.3	2.2	2.0	3.3	17.5	4.3	7.1	1.4	2.0	2.6	31.3	18.7	21.6	71.6	$138 - 10$
$A^k_{lh} = 0 A_{\rm DM} \neq 0$	6.0	11.3	2.2	4.0	2.7	6.6	6.5	6.4	2.8	22.2	5.8	6.9	1.5	2.0	2.5	40.2	28.3	21.0	89.5	$138 - 5$
$A^k_{lh} \neq 0 A_{\rm DM} = 0$	6.9	10.7	3.8	4.7	2.2	5.8	2.2	1.9	3.4	16.8	4.3	6.9	1.5	2.0	2.7	32.1	21.1	22.7	75.9	$138 - 8$
$A^k_{lh} = 0 A_{\rm DM} = 0$	6.1	14.9	4.5	6.6	2.6	6.2	7.4	6.3	2.8	19.5	5.4	6.8	1.5	2.0	2.6	41.1	31.2	23.0	95.3	$138 - 3$

Note. The number of degrees of freedom, $N_{\rm dof}$, is expressed as the total number of data points minus the number of free parameters in the fit.

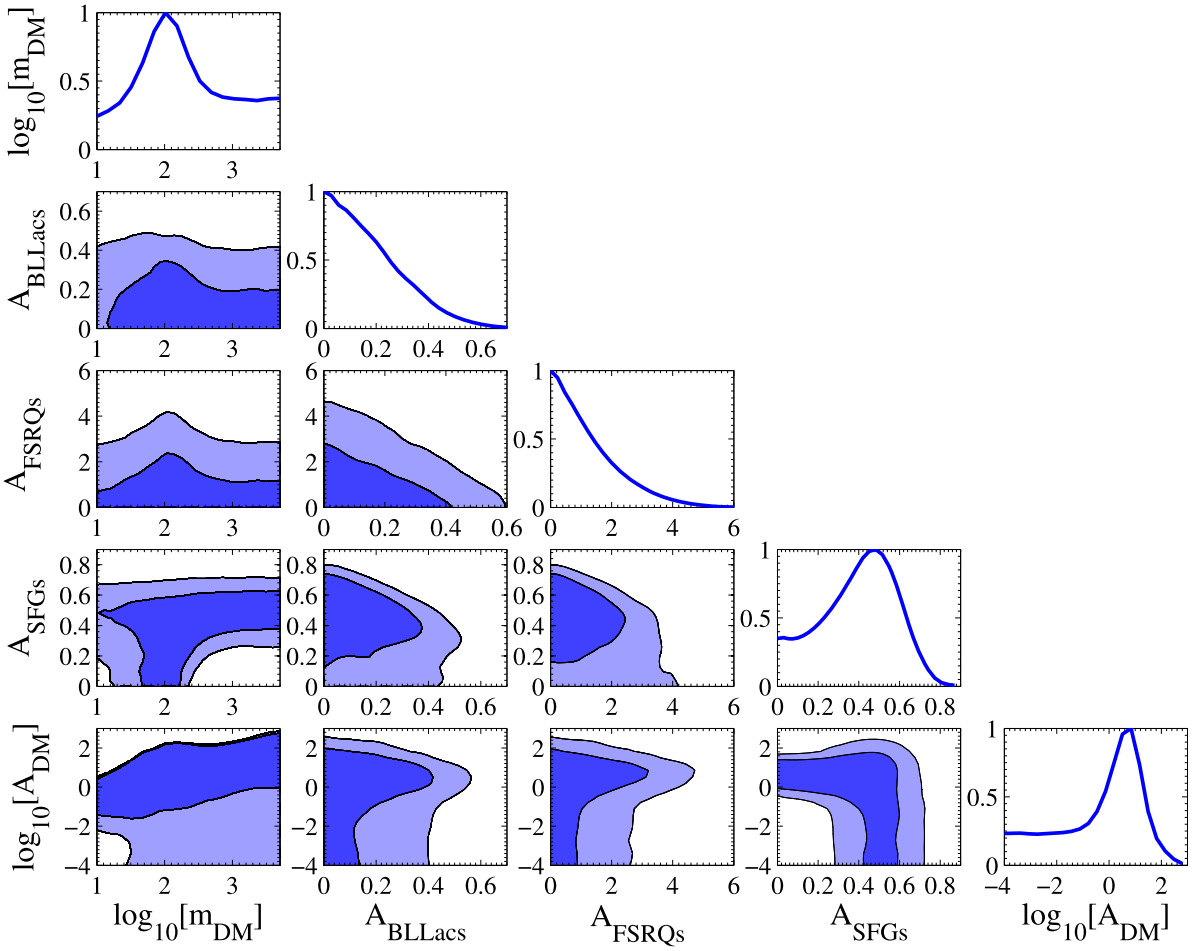

Figure 7. Triangle plot for the NVSS-6, $A_{1h}^{k} = 0$, $A_{\rm mAGN} = 0$ fit. The results refers to the $b\bar{b}$ annihilation channels and the LOW DM substructure scheme.

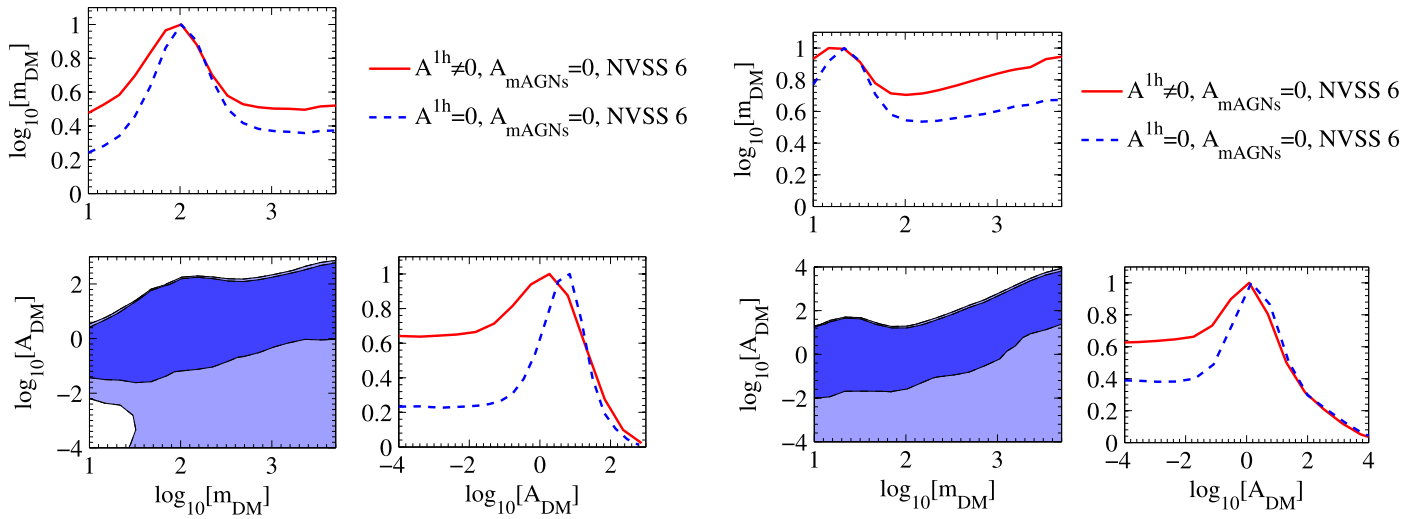

Figure 8. Left: detail from Figure 7 showing the DM parameters only. Furthermore, the 1D posterior panels show both the $A_{1h}^{k} = 0$ and $A_{1h}^{k} \neq 0$ cases. The plot refers to the $b\bar{b}$ annihilation channels and the LOW DM substructure scheme. Right: the same as in the left panel, but for the $\tau^{+}\tau^{-}$ annihilation channel.

about a factor of 4. The gain is significant and will further improve once the DM-mAGN-SFG degeneracies discussed above will be removed.

As expected, uncertainties on the bounds driven by the substructure model are significant. The left panel of Figure 10 shows that assuming the HIGH model would strengthen the constraints on the cross section by about one order of magnitude, whereas in the NS scenario the bounds would weaken by about a factor of 5. This implies that the thermal annihilation rate $\langle \sigma_a v \rangle = 3 \cdot 10^{-26}\,\mathrm{cm^3\,s^{-1}}$ is excluded at the 95% level up to masses of 6, 25, and 250 GeV in the NS, LOW, and HIGH scenarios, respectively.

In Figure 11 we instead show the 95% lower bounds on the lifetime of a decaying DM particle for various decay final

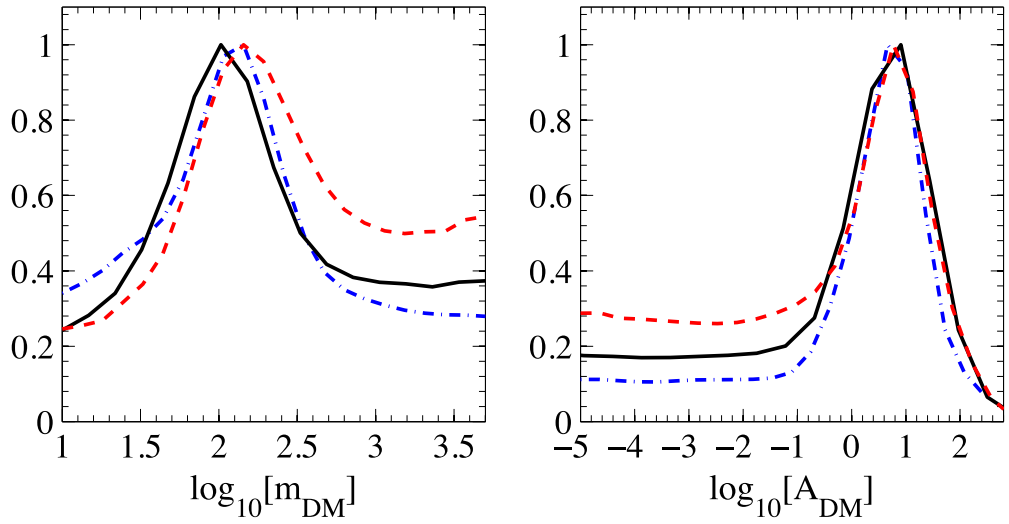

Figure 9. Comparison of the posteriors distributions for the DM parameters (mass $m_{\rm DM}$ (left) and annihilation rate in terms of the thermal one $A_{\rm DM}$ (right)) for the NVSS-6, $A_{1h}^{k}=0$, $A_{\rm mAGN}=0$ fit and for the three different SFG models described in the text.

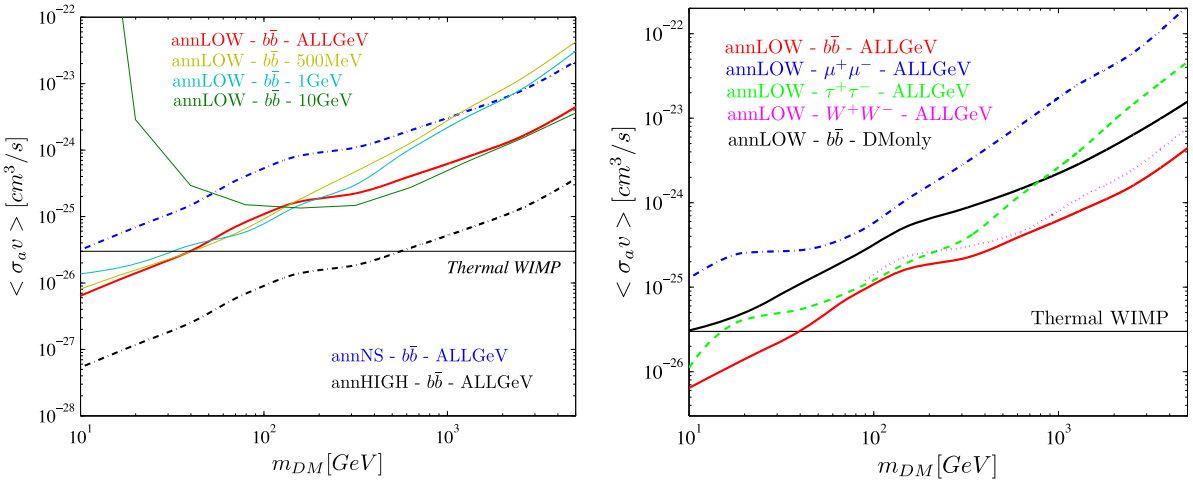

Figure 10. Left: 95% upper bounds on the DM annihilation rate $\langle\sigma_a v\rangle$ as a function of the DM mass, for the LOW substructures model and the reference NVSS-10 $A_{1h}^{k}\neq 0$ fit. Solid lines refer to the $b\bar{b}$ annihilation channel: the red line refers to the analysis that combines information from all the three energy bins under consideration ($E>0.5$, 1, 10 GeV), while the other three lines refer to the analysis performed on a single energy bin (as stated in the figure label). The upper dotted–dashed blue line refers to the NS substructure model, while the lower dotted–dashed black line to the HIGH substructure model. Right: in addition to the $b\bar{b}$ case (red line) reported in the left panel, the different lines show the upper bounds for the $\mu^{+}\mu^{-}$ (blue), $\tau^{+}\tau^{-}$ (green), and $W^{+}W^{-}$ (magenta) annihilation channels, for the LOW substructures model. The black line instead shows the upper bound for the $b\bar{b}$ case and LOW substructure scheme, obtained under the assumption that the DM contribution to the 2MASS cross-correlation is the dominant one (taken from Regis et al. 2015).

states. Bounds on DM decay, being proportional to the DM density (and not DM density squared, as instead the annihilation signal), depend on the total DM mass in structures and are not affected by the different substructure modeling. As for the annihilation case, including the astrophysical sources in the analysis improves the constraints, again by about a factor of 4, with respect to those obtained by ignoring the astrophysical components (Regis et al. 2015).

Finally, to test the robustness of our DM constraints, we have repeated the analysis using the same astrophysical models used in Xia et al. (2015) and we found that they are very similar to the ones obtained in the present analysis.

4.1. Self Consistency Rests: Mean Intensity and Auto-correlation of the IGRB

As anticipated in Section 3, instead of including the mean IRGB intensity and its auto-correlation in the fit, we use these additional observational inputs a posteriori as a self-consistent test for our best fitting model.

We define $A^{n}_{\rm IGRB}$, the fractional mean IGRB intensity predicted by the cross-correlation fit, as follows:

$$I^{n}_{\rm TOT}A^{n}_{\rm IGRB} = A_{\rm FSRQ}I^{n}_{\rm FSRQ} + A_{\rm BLLac}I^{n}_{\rm BLLac} + A_{\rm mAGN}I^{n}_{\rm mAGN} + A_{\rm SFG}I^{n}_{\rm SFG} + A_{\rm DM}I^{n}_{\rm DM}, \quad (8)$$

where I^{n}_{α} are the integrated γ-ray intensities of our *reference* models for the five γ-ray emitters considered here and shown in Figure 1 and $n=1$, 2, 3 identifies the energy band. The total intensity is defined as $I^{n}_{\rm TOT}\equiv\sum_{\alpha}I^{n}_{\alpha}$, where the sum runs over the five types of emitters. In our model $I^{n}_{\rm TOT}=10^{-6}$, 4×10^{-7}, $1.5\times10^{-8}\,{\rm cm^{-2}\,s^{-1}\,sr^{-1}}$ for the energy ranges $E>0.5$, 1, 10 GeV, respectively, which are consistent with the *measured* IGRB (Ackermann et al. 2015a). We thus expect that the $A^{n}_{\rm IGRB}$ have values close to unity to match observations.

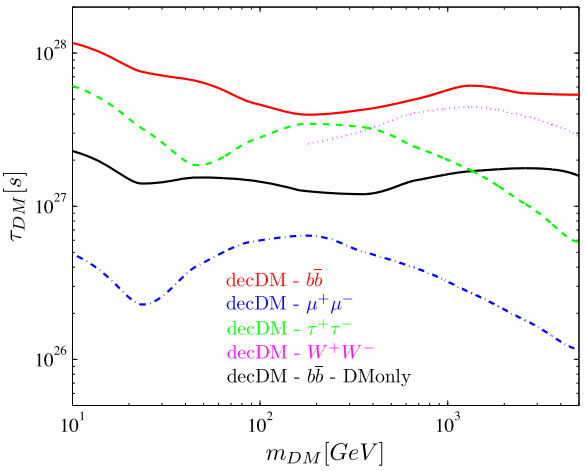

Figure 11. For a decaying DM, 95% lower limits on the DM lifetime τ as a function of its mass, for different decay channels: $b\bar{b}$ (red), $\mu^+\mu^-$ (blue), $\tau^+\tau^-$ (green), and W^+W^- (magenta). The black line instead shows the lower bound for the $b\bar{b}$ case obtained under the assumption that the DM contribution to the 2MASS cross-correlation is the dominant one (taken from Regis et al. 2015).

Note that the parameters $A^n_{\rm IGRB}$ need not to be the same in each energy band since the total signal $I^n_{\rm TOT}$ and the individual contributions I^n_α have different scaling in energy. However, the difference is not very large.

Similarly, we define the IGRB auto-correlation predicted from the cross-correlation fit, as a fraction of the measured one, in terms of the parameter $f_{C_{P,\rm IGRB}}$ as

$$C_{P,\rm TOT} f_{C_{P,\rm IGRB}} = A^2_{\rm FSRQ} C_{P,\rm FSRQ} + A^2_{\rm BLLac} C_{P,\rm BLLac} + A^2_{\rm mAGN} C_{P,\rm mAGN} + A^2_{\rm SFG} C_{P,\rm SFG}, \quad (9)$$

where $C_{P,\rm FSRQ} = 1.6 \times 10^{-18}$, $C_{P,\rm BLLac} = 7.9 \times 10^{-18}$, $C_{P,\rm mAGN} = 3.9 \times 10^{-19}$, and $C_{P,\rm SFG} = 6.3 \times 10^{-21}$, all of them in units of $(\rm cm^{-2}\,s^{-1}\,sr^{-1})^2 sr$. are the predicted average auto-correlation signals in the multipole range $\ell = 155$–504 and in the energy band 1–2 GeV. We have neglected the DM contribution since it is largely subdominant with respect to FSRQs, BL Lacs, and mAGNs (see Figure 1). The SFG contribution, which is also subdominant, is considered for the sake of completeness. In the above equation, we made the assumption that the amplitude of the auto-correlation signal scales with the square of the normalization parameters of the individual components. Unlike the cross-correlation case, we did not include any one-halo correction term since we model astrophysical emitters as point sources for which no additional small-scale power is expected to contribute to the auto-correlation signal. Like the mean intensity, the value $f_{C_{P,\rm IGRB}} = 1$ characterizes a model which saturates the measured IGRB auto-correlation.

In Figure 12 we show the posterior probabilities for $A^n_{\rm IGRB}$ in the three energy bands considered in our analysis and $f_{C_{P,\rm IGRB}}$. We find that the typical value $A_{\rm IGRB}$ is between 20% and 50% in the two lower energy bands (upper panels), whereas for $E > 10$ GeV is in the broader range 10%–80%. These results are robust to the details of the fitting procedure, as demonstrated by the similarity of the various curves. They imply that the extragalactic sources considered in our model (BL Lac, mAGN, SFG, FSRQ, and DM) which, as we have seen, provide a good match to the observed *cross correlation* with LSS tracers, also contribute to a significant fraction of the IGRB, although possibly not to the whole signal. This result is interesting but should also be taken with a grain of salt given the complexity of our cross-correlation model. For example, Xia et al. (2015), using a different model for the SFG emission and bias, was able to account for a larger fraction of the IGRB, although again not 100%. It should be also noted that the measurement of the IGRB in Ackermann et al. (2015a) is affected by systematic errors induced by the imperfect model of the foreground Galactic emission, even if the size of this systematic uncertainty does not seem to be large enough to saturate our models to 100% of the total emission. If indeed it turns out that additional γ-ray sources are required to explain the total intensity of the IGRB, then the results of our analysis set a rather sever constraint: their correlation with LSS tracers must be weak. This would imply that they should be local, possibly of Galactic origin, like the millisecond pulsar or perhaps diffuse inverse Compton photons from cosmic-ray electrons scattering on the optical/infrared Galactic inter-stellar radiation field. Future analyses with newer and additional data sets will help to clarify this interesting issue.

The posterior for $f_{C_{P,\rm IGRB}}$ is instead consistent with unity, although its probability distribution actually spans several orders of magnitude from 10^{-2} to 10, meaning that the measured auto-correlation does not provide a very stringent cross-check.

5. SUMMARY AND CONCLUSIONS

In this paper, we have used the cross-correlations recently measured in Xia et al. (2015) between *Fermi*-LAT diffuse γ-ray maps and different catalogs of LSS tracers to investigate the origin of the IGRB and the nature of the various sources that may contribute to it, including DM annihilation or decay. This work extends that of Regis et al. (2015), which used only the γ-ray-2MASS correlation and considered DM as the only source of the extragalactic γ-ray signal. Our main results are as follows.

1. Our theoretical models provide a good fit to the cross-correlation measured in all employed catalogs of extragalactic tracers, namely SDSS-DR6 quasars, 2MASS, NVSS, SDSS-DR8 LRGs, and SDSS-DR8 MG. The quality of the fit is quantified by means of a χ^2 analysis in which we account for covariance among the errors in different angular bins, whereas we ignore the covariance among energy bins and among the different catalogs. The first approximation is justified by the photon statistics, which is dominated by low-energy event, making each of the energy bins considered in our analysis effectively independent. The second approximation is justified by the spatial distributions of the objects in the different catalogs that, with the partial exception of the NVSS one, do not significantly overlap with each other.
2. In our CCF models we consider four different types of astrophysical sources (two flavours of blazars, FSRQs and BL Lacs, SFGs, and mAGNs) and, in addition, annihilating/decaying DM. The rationale behind the choice of these astrophysical sources is that previous analyses have shown that they are the main contributors to the IGRB and its angular auto-correlation. These two observational constraints are not considered in our fit.

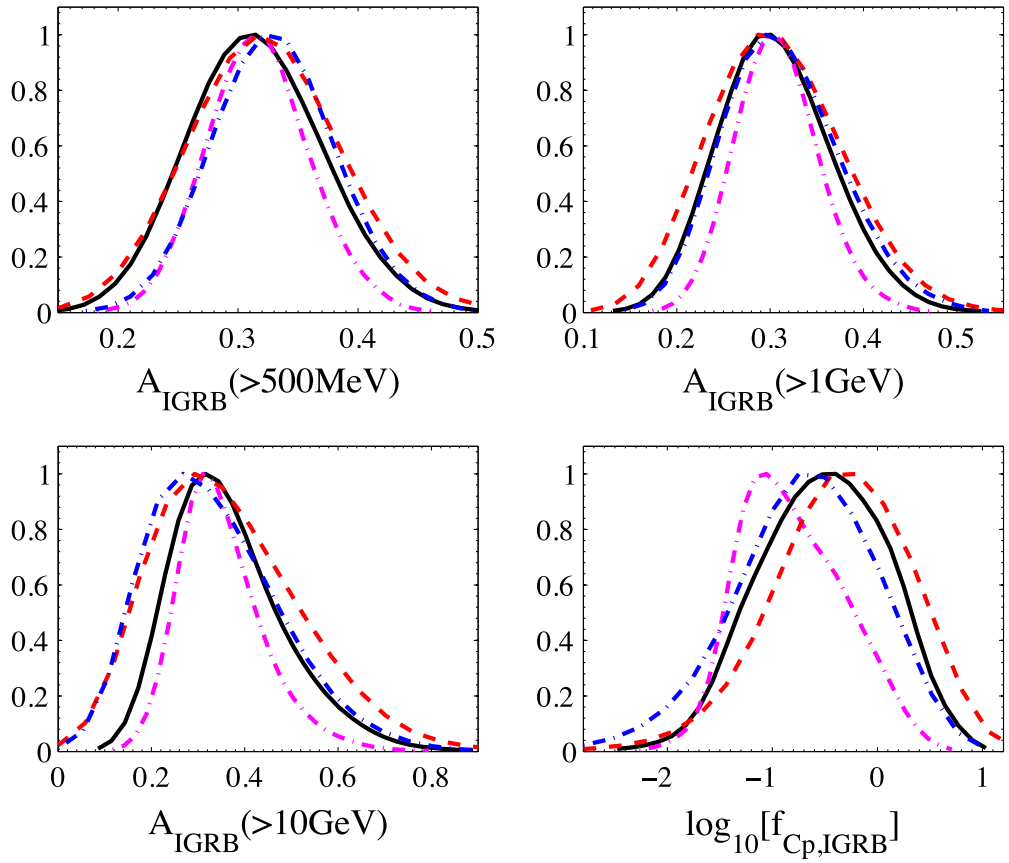

Figure 12. Marginalized 1D posterior probabilities for the cumulative fractional contribution $A_{\rm IGRB}$ of all γ-ray sources (BL Lac, mAGN, SFG, FSRQ, and DM) to the total intensity $I_{\rm IGRB}$ measured by *Fermi*. $A_{\rm IGRB}$ is expressed in terms of $I_{\rm IGRB} = 10^{-6}$, 4×10^{-7}, 1.5×10^{-8} cm^{-2} s^{-1} sr^{-1} for the energy bins $E > 0.5$, 1, 10 GeV (to account for spectral behavior). The bottom right panel shows the same information for the IGRB angular auto-correlation in the 1–2 GeV energy band. The various lines refer to the four fits described in the text with same color and dashing conventions of Figure 6.

Instead, we use them a posteriori to check the consistency of our best fitting models which are based solely on the measured CCF. We find that models that provide a good match to the cross-correlation fall short of accounting for the mean γ-ray intensity. The discrepancy is not large, less than a factor of 2, especially in the high-energy band, and could be accounted for by a combination of model uncertainty and imperfect subtraction of the Galactic foreground. However, it may also indicate that additional types of sources that do not cross-correlate with the LSS, like γ-ray sources within our Galaxy, are required to account for the whole IGRB intensity.

3. Including DM among the possible IGRB sources does not significantly improve the quality of the fit, and does not indicate a preference for a particular DM mass or annihilation cross section/decay rate. We find that the reason for the low statistical significance on the presence of a DM component does not lie in the fact that the fit rejects this component, while it is rather due to the presence of a model degeneracy with other types of astrophysical sources, mainly mAGNs and SFGs. In other words, a significant DM contribution gives an equally good fit as a case with a negligible DM contribution and a larger mAGNs and SFGs emission. Neglecting the mAGN component in the fit partially breaks this degeneracy and provides a small ($\sim 2\sigma$) preference for DM. The best fit is found for a rather canonical WIMP DM candidate with $m_{\rm DM} \sim 100$ GeV that annihilates into $b\bar{b}$ at a rate which is of the order of the thermal value for the benchmark LOW DM clustering scenario considered. A candidate with a slight smaller mass of about 30 GeV that annihilates into $\tau^+\tau^-$ provides an equally good fit.
4. Breaking this degeneracy is the main goal of future cross-correlation analyses similar to the present one. Fortunately, this is a realistic goal. One of the main reasons for this degeneracy is the uncertainty on the mAGN and SFG luminosity in γ-ray which, to date, has been directly measured for a handful of very nearby objects. However, their number is bound to increase due to the fact that *Fermi*-LAT will keep taking data in the next few years. In addition, the quality of the *Fermi* maps is also expected to increase both in terms of photon statistics, which will allow to better sample the energy behavior and to improve the sensitivity to characteristic DM spectral features, and angular resolution, which would allow us to push the correlation analysis to smaller angular scales where the one-halo term dominates.
5. We turn the non-detection of DM into limits on the annihilation cross section/decay rate as function of the DM mass. Our derived constraints are comparable in strenght to most of the current indirect detection method that exploits the γ-ray sky (Regis et al. 2015). These constraints are rather robust to the astrophysical details of the models but, as expected, do depend on the detail of the DM substructure and small-scale clustering. For this reason and with the aim of bracketing current theoretical

uncertainties, in addition to the LOW scenario which represents the current, somewhat conservative, benchmark substructure model, we have explored two additional, rather extreme cases: the NS case in which we completely ignore substructures and that provides extremely conservative constraints of the DM properties, and the HIGH scenario in which substructures are more numerous and have an higher density concentration. In the most conservative NS scenario, our method excludes, at a credible level larger than 95%, that DM particles with masses smaller than 10 GeV annihilating entirely into $b\bar{b}$ could have a thermal cross section. In the optimistic scenario, the same statement applies to particles lighter than ∼600 GeV. The bounds are a factor of ∼4 stronger than the most conservative case considered in Regis et al. (2015) in which only DM is used in order to saturate the 2MASS cross-correlation. Constraints on DM decay time for DM decaying into $b\bar{b}$ are $\sim 10^{28}$ s, roughly independently from the DM mass.

All in all, we are confident that the results obtained in our analysis, which are already quite remarkable considering that this is the first time that a genuine cross-correlation signal is detected in the *Fermi*-LAT γ-ray maps, will soon improve significantly. In this respect, this work also represents a proof of concept that illustrates the potential of the cross-correlation analysis. We base our optimism on the fact that the new Pass8 data, with improved effective area and angular resolution, will soon be released by the *Fermi*-LAT Collaboration and that additional catalogs of objects al relatively low redshifts with wide, almost all-sky, angular coverage and well determined redshift distribution are already available (Bilicki et al. 2014) and some new ones are being compiled (M. Bilicki 2015, private communication).

This work is supported by the research grant *Theoretical Astroparticle Physics* number 2012CPPYP7 under the program PRIN 2012 funded by the Ministero dell'Istruzione, Università e della Ricerca (MIUR), by the research grants *TAsP (Theoretical Astroparticle Physics)* and *Fermi* funded by the Istituto Nazionale di Fisica Nucleare (INFN), and by the *Strategic Research Grant: Origin and Detection of Galactic and Extragalactic Cosmic Rays* funded by Torino University and Compagnia di San Paolo. M.V. and E.B. are supported by PRIN MIUR and IS PD51 INDARK grants. M.V. is also supported by ERC-StG cosmoIGM, PRIN INAF. J.X. is supported by the National Youth Thousand Talents Program, the National Science Foundation of China under Grant No. 11422323, and the Strategic Priority Research Program, *The Emergence of Cosmological Structures* of the Chinese Academy of Sciences, grant No. XDB09000000.

APPENDIX A
WINDOW FUNCTIONS

In this appendix, we discuss the modeling of the window functions adopted for the calculation of the cross-correlation angular PS $C^{\gamma g}$ of Equation (1), which are in turn the ingredient for the determination of the cross-correlation function $\mathrm{CCF}^{\gamma g}(\theta)$ defined in Equation (4).

A.1. DM

A.1.1. Annihilating DM

DM annihilations in haloes and in their substructures produce γ-ray photons. This emission traces the DM density squared $\rho^2_{\rm DM}$: therefore the density field responsible for the correlation signal is $f_{\delta^2}(\chi, \boldsymbol{r}) = \rho^2_{\rm DM}(\chi, \boldsymbol{r})$. The window function reads

$$W_{\delta^2}(\chi) = \frac{\left(\Omega_{\rm DM}\rho_c\right)^2}{4\pi}\frac{\langle\sigma_a v\rangle}{2m^2_{\rm DM}}[1+z(\chi)]^3\Delta^2(\chi) \times \int_{E_\gamma > E_{\rm min}} dE_\gamma \frac{dN_a}{dE_\gamma}\left[E_\gamma(\chi)\right]e^{-\tau\left[\chi, E_\gamma(\chi)\right]}, \quad (10)$$

where $\Omega_{\rm DM}$ is the cosmological abundance of DM, ρ_c is the critical density of the universe, $m_{\rm DM}$ is the mass of the DM particle, and $\langle\sigma_a v\rangle$ denotes the velocity-averaged annihilation rate, assumed here to be the same in all halos. dN_a/dE_γ indicates the number of photons produced per annihilation event, and sets the γ-ray energy spectrum. We will consider annihilation into $b\bar{b}$ quarks as representative of a typical soft annihilation spectrum (with γ-rays mostly arising from production and decay of neutral pions), and into $\mu^+\mu^-$ leptons as representative of a hard-spectrum channel (where γ-rays mostly arising from final state radiation), with $\tau^+\tau^-$ and W^+W^- final states as intermediate possibilities. $E_{\rm min}$ is the energy threshold of the *Fermi*-LAT maps considered in the analysis, namely: $E_{\rm min} = 0.5,\ 1,\ 10$ GeV. The factor $\exp\{-\tau[\chi, E_\gamma(\chi)]\}$ accounts for absorption due to the extragalactic background light, and we model the optical depth τ as in Franceschini et al. (2008).

A crucial quantity in Equation (10) is the so-called clumping factor $\Delta^2(\chi)$:

$$\Delta^2(z) \equiv \frac{\left\langle\rho^2_{\rm DM}\right\rangle}{\bar{\rho}^2_{\rm DM}} = \int_{M_{\rm min}}^{M_{\rm max}} dM \frac{dn}{dM}(M, z) \times \left[1 + b_{\rm sub}(M, z)\right]\int d^3\boldsymbol{x}\ \frac{\rho^2_h(\boldsymbol{x}|M, z)}{\bar{\rho}^2_{\rm DM}}. \quad (11)$$

The clumping factor involves the integral of the halo number density dn/dM above the so-called minimal halo mass $M_{\rm min}$, multiplied by the total number of annihilations produced in the generic haloes of mass M at redshift z with density profile $\rho_h(\boldsymbol{x}|M, \chi)$ and with subhalos providing a "boost" to the emission given by $b_{\rm sub}$. We assume a reference value of $10^{-6}\,M_\odot$ for $M_{\rm min}$, which corresponds to a typical free-streaming mass in the WIMP DM scenario. We adopt the halo mass function from Sheth & Tormen (1999) and we assume that the halos are characterized by the so-called Navarro–Frenk–White (NFW) universal density profile (Navarro et al. 1997). The profile is completely determined by the total mass of the halo and by its size. We express the latter in terms of the concentration parameter $c(M, z)$, taken from Prada et al. (2012; see also Sanchez-Conde & Prada 2014 for an analytic fit of $c(M, z = 0)$ of Prada et al. 2012).

Concerning the boost provided by subhalos hosted in the main halos, we consider three scenarios (HIGH, LOW, and NS) as extreme cases bracketing the effect. In Equation (11) this is

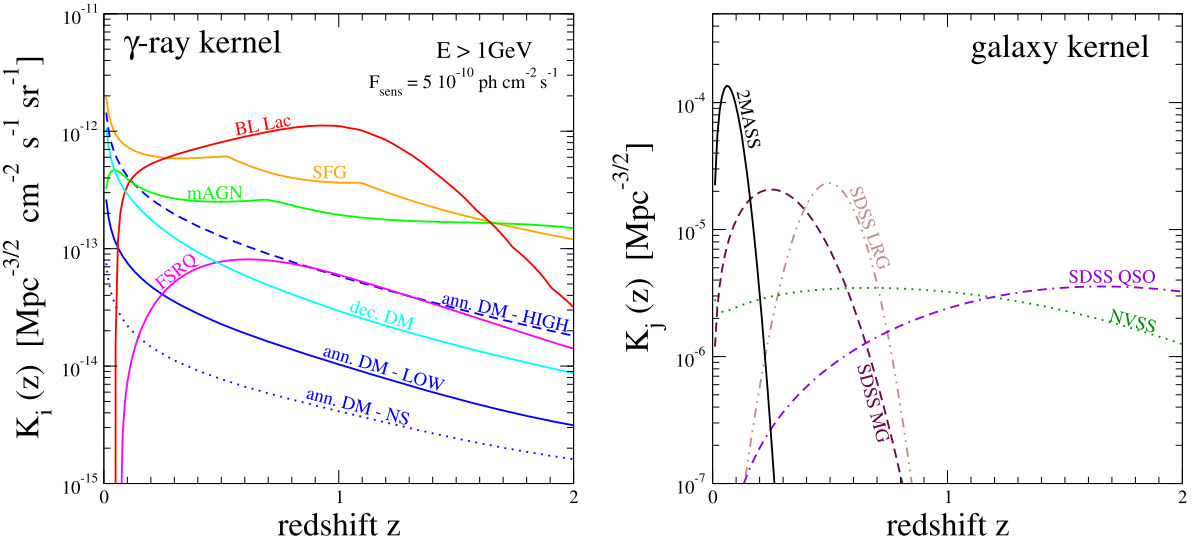

Figure 13. Angular-power-spectrum kernels $K(z)$ of γ-ray emitters (left) and galaxies (right), shown as a function of the redshift z. The kernel is defined as $K_a(z) = \sqrt{c\, z/H(z)}\, W_a(z)/\chi(z)$, where $H(z)$ is the Hubble parameter, $W_a(z)$ denotes the window function of the objects of class a and χ is the comoving distance. The γ-rays kernels are integrated for energies above 1 GeV and refer to unresolved sources fainter than $F_{\rm sens} = 5 \cdot 10^{-10}$ photons cm^{-2} s^{-1}.

indeed the most uncertain quantity (Gao et al. 2012; Fornasa et al. 2013; Ng et al. 2014; Sanchez-Conde & Prada 2014). In the LOW scenario, the function $b_{\rm sub}(M, z)$ is computed following Sanchez-Conde & Prada (2014; see, in particular, their Equation (2) assuming a subhalo mass function $dn/dM_{\rm sub} \propto M_{\rm sub}^{-2}$). The HIGH scenario stems instead from the $b_{\rm sub}(M, z)$ found in Gao et al. (2012), and assuming no redshift dependence. In the NS case, we simply set $b_{\rm sub} = 0$: this can be considered as the most conservative approach.

The blue curves in Figure 13(a) show a quantity related to the window function of Equation (10), defined as the kernel of the γ-ray emission entering in the computation of the angular PS discussed in Section 2. Specifically, we define the kernels as

$$K_a = \sqrt{c\, z/H(z)}\, W_a(z)/\chi(z), \tag{12}$$

such that

$$C_\ell^{(\gamma_i g_j)} = \int d\, \ln(z) K_{\gamma_i}(z)\, K_{g_j}(z)\, P_{\gamma_i g_j}(k, z). \tag{13}$$

In Figure 13(a) we choose a reference particle-physics model with $m_{\rm DM} = 100$ GeV, $\langle \sigma_a v \rangle = 3 \times 10^{-26}$ cm^3 s^{-1} and $b\bar{b}$ annihilation channel. The three clustering scenarios (NS, LOW, and HIGH for dotted, solid, and dashed curves, respectively) share approximately the same redshift dependence, but they correspond to different sizes of the clumping factor and consequently of the intensity of the DM-induced γ-ray flux. Note that a comparison with previous works in the literature can be non-trivial, as different groups employ different prescriptions for the ingredients of the DM clustering and, in particular, for the boost factor. Figure 13 can be useful also as a normalization test when confronting the results presented in the rest of the paper with other works.

A.1.2. Decaying DM

If instead of being stable, the DM particles decay, while having a negligible self-annihilation rate, the produced γ-rays traces the DM density linearly, i.e., $f_\delta(\chi, \boldsymbol{r}) = \rho_{\rm DM}(\chi, \boldsymbol{r})$, The window function in this case reads

$$W_\delta(\chi) = \frac{\Omega_{\rm DM}\rho_c}{4\pi} \frac{\Gamma_{\rm d}}{m_{\rm DM}} \int_{E_\gamma > E_{\rm min}} \times\, dE_\gamma \frac{dN_d}{dE_\gamma}\big[E_\gamma(\chi)\big] e^{-\tau\left[\chi, E_\gamma(\chi)\right]}, \tag{14}$$

where $\Gamma_{\rm d}$ is the decay rate. The photon yield, dN_d/dE_γ, is assumed to be the same as for annihilating DM, but with the energy of the process given by $\sqrt{s} = m_{\rm DM}$ instead of $2m_{\rm DM}$. In other words, $dN_d/dE_\gamma(E_\gamma) = dN_a/dE_\gamma(2E_\gamma)$ with the kinematic end-point being at $m_{\rm DM}/2$. The kernel in the case of decaying DM is shown as a cyan curve in Figure 13(a). In the plot we report reference particle-physics model with $m_{\rm DM} = 200$ GeV, $\tau_{\rm d} = 1/\Gamma_{\rm d} = 6 \times 10^{27}$ s and decays into $b\bar{b}$ quarks. Note that for decaying DM, the window function does not depend on the details of the DM clustering. We note also that DM kernels peak at low redshifts, for both annihilating and decaying DM, and have a relative fast decrease with distance.

A.2. Astrophysical Sources

For astrophysical sources, we adopt as the characterizing parameter the source γ-ray luminosity $\mathcal{L}$ in the energy interval (0.1–100) GeV. For a power-law energy spectrum with spectral index α, the window function takes the form

$$W_{S_i}(\chi) = \frac{(\alpha_i - 2)\left\langle f_{S_i}(\chi)\right\rangle}{4\pi E_0^2\, [1 + z(\chi)]^2} \int_{E_\gamma > E_{\rm min}} \times\, dE_\gamma \left(\frac{E_\gamma}{E_0}\right)^{-\alpha_i} e^{-\tau\left[\chi, E_\gamma(\chi)\right]}, \tag{15}$$

where $E_0 = 100$ MeV is just the normalization energy, and i stands for each of the γ-rays sources adopted in our analysis: BL Lac, FSRQ, mAGN, and SFG. The mean luminosity produced by an unresolved class of objects located at a distance

χ from us is denoted by $\langle f_{S_i}(\chi)\rangle$ and is given by:

$$\langle f_{S_i}(\chi)\rangle = \int_{\mathcal{L}_{\rm min,i}}^{\mathcal{L}_{\rm max}(F_{\rm sens},z)} d\mathcal{L}\, \mathcal{L}\, \Phi_i(\mathcal{L}, z), \quad (16)$$

where $\Phi_i(\mathcal{L}, z)$ is the γ-ray luminosity function for the source class i. The upper bound, $\mathcal{L}_{\rm max}(F_{\rm sens}, z)$, is the luminosity above which an object can be resolved, given the detector sensitivity $F_{\rm sens}$ for which we assume the value $F_{\rm sens} = 5 \times 10^{-10}$ photons cm^{-2} s^{-1} above 1 GeV (Nolan et al. 2012; Acero et al. 2015). The precise value depends slightly on α_i and on the catalog of resolved point sources, although varying $F_{\rm sens}$ within these different values has only a weak impact of the window function. Conversely, the minimum luminosity $\mathcal{L}_{{\rm min},i}$ depends on the properties of the source class under investigation. The four populations of astrophysical γ-ray emitters (i.e., BL Lac, FSRQ, mAGNs, and SFGs) are discussed in the following. For each of them we describe the choice of α_i and of the γ-ray luminosity function.

A.2.1. Blazars

We consider BL Lacertae (BL Lacs) and FSRQ separately. The γ-ray luminosity function of BL Lacs and FSRQ is taken from Ajello et al. (2012, 2014), respectively, where it is derived from a parametric fit of the redshift and luminosity distributions of resolved blazars in the *Fermi*-LAT catalog. The lower limit of the integral in Equation (16) is set to $\mathcal{L}_{\rm min} = 7 \cdot 10^{42}$ erg s^{-1} (BL Lac) and $\mathcal{L}_{\rm min} = 4 \cdot 10^{43}$ erg s^{-1} (FSRQ). For the energy spectrum, we consider a simple power law with a spectral index taken from the average spectral index in Ajello et al. (2012, 2014), namely, we assume $\alpha_{\rm BL\,Lac} = 2.1$ and $\alpha_{\rm FSRQ} = 2.44$.

The kernels of unresolved blazars are shown by the solid red (BL Lac) and magenta (FSRQ) lines in Figure 13(a). Note that they strongly decrease at low z since *Fermi*-LAT has already detected a large number of the closest (brightest) emitters of these classes.

A.2.2. Misaligned AGNs

In the case of mAGN, we follow Di Mauro et al. (2014a), which studied the correlation between the γ-ray luminosity and the core radio luminosity $L_{r,\rm core}$ at 5 GHz, and derived the GLF from the radio luminosity function. We consider their best-fit $\mathcal{L}$ versus $L_{r,\rm core}$ relation and assume an average spectral index $\alpha_{\rm mAGN}$ of 2.37. The solid green line in Figure 13(a) indicate the contribution of unresolved mAGNs.

A.2.3. SFGs

As in Ackermann et al. (2012b), we assume that the γ-ray and infrared (IR) luminosities are correlated in the case of SFG. We adopt the best-fit $\mathcal{L}$ versus $L_{\rm IR}$ relation from Ackermann et al. (2012b), while for the IR luminosity function we adopt the one from Gruppioni et al. (2013; adding up spiral, starburst, and SF-AGN populations of their Table 8), as considered in Tamborra et al. (2014). The spectral index is taken to be $\alpha_{\rm SFG} = 2.7$ for all the three components although starbursts galaxies would require in principle a somewhat harder spectrum. Nonetheless, this component is subdominant in the total SFG contribution except for high energies and at high redshift (i.e., in the ranges which are less relevant for the analyses in our work). The above choice thus has no practical effects on our results. The kernel associated with unresolved SFGs is the solid orange line in Figure 13(a). All the different single peaked sub-populations provide sizable contributions and this gives raise to different peaks.

The γ-ray emission produced by the four extragalactic astrophysical populations described above accounts for approximately the whole IGRB and auto-correlation angular PS (see Figure 1). As described in the main text, we, however, introduced a normalizing constant A_α for each population to be determined by the fit. Apart from the extragalactic DM-induced emission described in Appendices A.1.1 and A.1.2, there may be a contribution associated with annihilations/decays in the DM halo of the Milky Way. This is not included since it does not correlate with the LSS tracers.

A.3. Galaxy Catalogs

For galaxies, we take the redshift distributions $dN_j/dz(\chi)$ reported in Xia et al. (2015). The associated kernels are shown in Figure 13(b). The 2MASS kernel peaks at low redshift, and a comparison with the γ-rays kernels shown in the left panel of the same Figure 13 indicates that the 2MASS catalog is the most suitable for investigating a DM signal in the cross-correlation analysis, followed by the SDSS Main Galaxy Sample catalog.

APPENDIX B
HOD OF GALAXIES

In this work, we compute the angular cross-correlation between the unresolved γ-ray sky and the number of galaxies in specific catalogs. In order to estimate the latter from a theoretical point of view (and since we adopt the halo model description for the structure clustering), we need to describe how galaxies populate halos. Namely, we need to model how many galaxies of a certain catalog are present in a halo of mass M and how they are spatially distributed. To this aim, we employ the HOD formalism.

We follow the approach described in Zheng et al. (2005; for a review on HOD, see also Berlind & Weinberg 2002; Cooray & Sheth 2002), where the HOD is parameterized by distinguishing the contributions of central and satellite galaxies, $N = N_{\rm cen} + N_{\rm sat}$ (since different formation histories typically imply different properties for galaxies residing at the centers of halos with respect to satellite galaxies). These can be modeled with the following functional forms:

$$\langle N_{\rm cen}(M)\rangle = \frac{1}{2}\left[1 + {\rm erf}\left(\frac{\log M - \log M_{\rm th}}{\sigma_{\log M}}\right)\right] \quad (17)$$

$$\langle N_{\rm sat}(M)\rangle = \left(\frac{M}{M_1}\right)^{\alpha} \exp\left(-\frac{M_{\rm cut}}{M}\right). \quad (18)$$

With this formalism, we need five parameters for each galaxy population: $M_{\rm th}$ denotes the approximate halo mass required to populate the halo with the considered type of galaxies, with the transition from 0 to 1 central galaxy modeled by means of Equation (17), and set by the width $\sigma_{\rm Log\,M}$. The satellite occupation is described by a power law (with index α and normalization set by the mass M_1), with an exponential cutoff $M_{\rm cut}$ at low masses. The value of the five HOD parameters for each of the considered galaxy population is discussed in the

following. For some catalogs, we will also consider similar but slightly different functional forms.

We selected those galaxy samples with available HOD which more closely resemble the catalogs considered in the cross-correlation analysis of this work. We caution, however, that since the matching of the two samples is not perfect some differences in the associated HODs might be expected. Nevertheless, this should not affect our results in a dramatic way.

Equations (17) and (18) provide the number of galaxies in a halo of mass M. Concerning the spatial distribution, we treat central and satellite galaxies separately. The former is taken as a point source located at the center of the halo (the point source approximation is expected to break down only for $\ell \gtrsim 10^3$). Satellite galaxies are instead described in an effective way with a spatial distribution following the host halo profile. In other words, we express the density field of galaxies with

$$g_g(x - x'|M) = \langle N_{\rm cen}(M)\rangle\, \delta^3(x - x') + \langle N_{\rm sat}(M)\rangle\, \rho_h(x - x'|M)/M. \quad (19)$$

Note that

$$\int d^3x\, g_g(x) = \langle N_{\rm cen}(M)\rangle + \langle N_{\rm sat}(M)\rangle = \langle N(M)\rangle. \quad (20)$$

B.1. 2MASS HOD

A determination of the HOD for the 2MASS galaxies is not present in the literature (to the knowledge of the authors). In Zehavi et al. (2005), a sample of about 200,000 SDSS galaxies mostly residing in the redshift range $0.02 < z < 0.167$ and with r-band magnitude $14.5 \leqslant r \lesssim 17.77$ was analyzed. Such ranges of redshift and magnitude are analogous to the ones of the adopted 2MASS catalog (Jarrett et al. 2000), with the cross-identification of the latter with SDSS found to be successful for about 90% of the sources (McIntosh et al. 2006). We can thus exploit the HOD results of Zehavi et al. (2005). They considered a step function ($\langle N_{\rm cen}\rangle = 0$ for $M < M_{\rm th}$ and $\langle N_{\rm cen}\rangle = 1$ for $M \geqslant M_{\rm th}$) instead of Equation (17), and set $M_{\rm cut} = 0$ in Equation (18). The analysis was performed by splitting the sample in luminosity bins, but for our purposes we can consider the averaged best-fit parameters weighted over the number of galaxies in each bin. We found $\log M_{\rm th} = 12.1$,$\alpha = 1.2$, and $\log M_1 = 13.5$.

B.2. NVSS HOD

The NVSS subsample considered in this work (Blake & Wall 2002) contains sources brighter than 10 mJy at 1.4 GHz. The vast majority of them is associated to bright AGNs. To model the AGN HOD, we follow Chatterjee et al. (2012). For bright objects, they found $\log M_{\rm th} = 13.03$, $\sigma_{\log M} = 0.96$, $\alpha = 1.17$, $\log M_{\rm cut} = 11.5$, and $\log M_1 = 13.64$.

B.3. SDSS-DR8 Main Galaxy Sample HOD

In Ross et al. (2010), the clustering of more than three million photometrically selected SDSS galaxies was analyzed. In particular, the sample was defined requiring de-reddened r-band magnitudes $r_d < 21$ and absolute magnitudes $M_r < -21.2$, in the redshift range $0.1 < z < 0.4$ and masking objects with Galactic extinction $A_r > 0.2$. This galaxy sample is very similar to the one adopted in this work for the cross-correlation analysis (Aihara et al. 2011), except for a more limited redshift (and magnitude) range. Since the peak of the redshift distribution is at $z \sim 0.3$, such difference is not expected to play a major role. After averaging the best-fit values of HOD parameters over the different redshift bins considered in Ross et al. (2010; weighted for the number of galaxies in each bin), we obtain $\log M_{\rm th} = 12.09$, $\sigma_{\log M} = 0.3$, $\alpha = 1.09$, and $\log M_1 = 13.25$. The functional form of the satellite HOD considered in Ross et al. (2010) is

$$\langle N_{\rm sat}\rangle = \langle N_{\rm cen}\rangle \times \left(\frac{M - M_{\rm th}}{M_1}\right)^{\alpha} \quad (21)$$

instead of Equation (18), with $\langle N_{\rm cen}\rangle$ from Equation (17) and $\langle N_{\rm sat}\rangle = 0$ for $M < M_{\rm th}$.

B.4. SDSS-DR8 LRG HOD

A recent analysis of more than 50,000 SDSS-III CMASS galaxies (Reid et al. 2014) derived the HOD of this galaxy sample. The satellite HOD was modeled by means of

$$\langle N_{\rm sat}\rangle = \langle N_{\rm cen}\rangle \times \left(\frac{M - M_{\rm cut}}{M_1}\right)^{\alpha}, \quad (22)$$

with $\langle N_{\rm cen}\rangle$ given by Equation (17) (and $\langle N_{\rm sat}\rangle = 0$ for $M < M_{\rm cut}$). The best-fit parameters in the fiducial model of Reid et al. (2014) are $\log M_{\rm th} = 13.03$, $\sigma_{\log M} = 0.38$, $\alpha = 0.76$, $\log M_1 = 14.08$, and $M_{\rm cut} = 13.27$. These results are found to be in agreement with the HOD analysis presented in White et al. (2011), which in turn was tested to reproduce the clustering of the galaxy sample of Ho et al. (2012) adopted here.

B.5. SDSS-DR6 Quasar HOD

The modeling of the HOD of SDSS quasars is taken from Richardson et al. (2012). The sample consists of 47,699 quasars in the redshift range $0.4 < z < 2.5$ with median redshift of $\bar{z} = 1.4$ and flux limited to $i < 19.1$. It is very similar to the catalog considered in this work for the cross-correlation analysis (Richards et al. 2009). The best-fit parameters entering in Equations (17) and (18) are not provided in Richardson et al. (2012), but we find that with $\log M_{\rm th} = 16.5$, $\sigma_{\log M} = 1.65$, $\alpha = 1$, $\log M_{\rm cut} = 15.25$, and $\log M_1 = 13.1$, the best-fit curve in their Figure 2(b) is well reproduced.

APPENDIX C
3D POWER SPECTRA

In the halo model computation of the cross-correlation PS, the 3D PS is split in the one-halo (P^{1h}) and two-halo (P^{2h}) components with $P = P^{1h} + P^{2h}$. For a derivation of the P^{1h} and P^{2h} discussed in the equations below, see Fornengo & Regis (2014). We remind that S_i denote γ-ray astrophysical emitters (BL Lac, FSRQ, mAGN, and SFG), g_j are associated to and galaxy populations (SDSS-DR6 quasars, 2MASS galaxies, NVSS radio sources, SDSS-DR8 LRG, and SDSS-DR8 "main" galaxies), while δ and δ^2 stands for decaying and annihilating DM, respectively. In most of the equations, the dependence on z is not explicitely reported to simplify the notation.

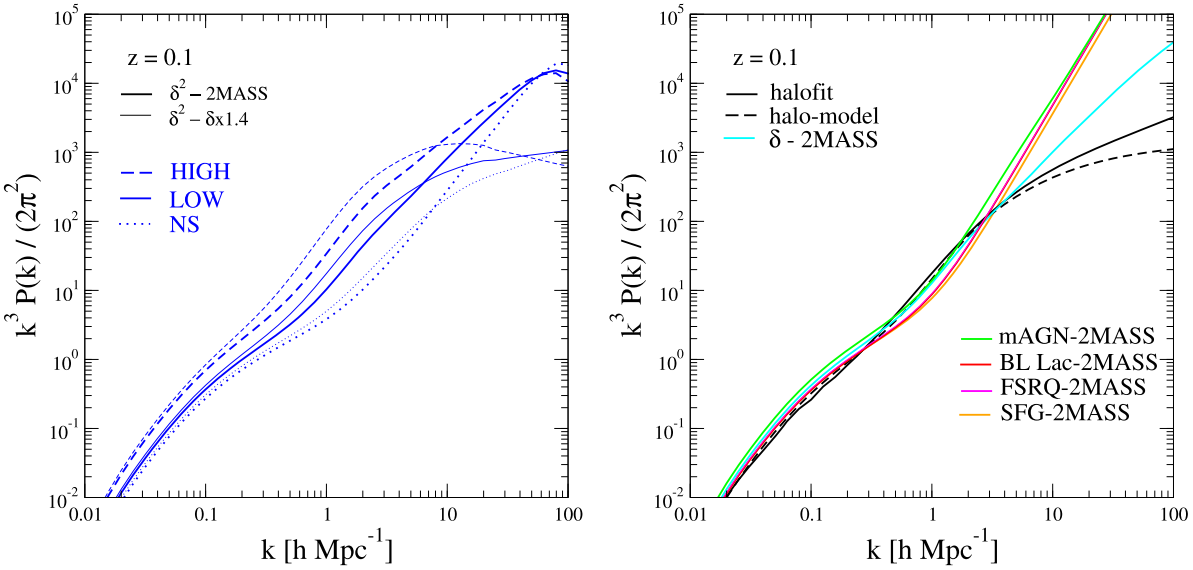

Figure 14. Power spectrum (multiplied by k^3) of cross-correlation between γ-ray emitters and 2MASS galaxies at redshift $z = 0.1$. The left panel refers to annihilating DM. The right panel shows decaying DM and astrophysical sources. The matter power spectrum obtained within the halo model employed in this work is shown with a dashed black line and is compared with the halofit results (Takahashi et al. 2012) derived from high-resolution N-body simulations (black solid line).

The 3D PS of cross-correlation between γ-rays from annihilating DM and galaxy catalogs is computed as

$$P^{1h}_{g_j,\delta^2}(k,\,z) = \int_{M_{\rm min}}^{M_{\rm max}} dM\ \frac{dn}{dM}\frac{\left\langle N_{g_j}\right\rangle}{\bar{n}_{g_j}}\tilde{v}_g(k\,|M)\,\frac{\tilde{u}(k\,|M)}{\Delta^2} \quad (23)$$

$$P^{2h}_{g_j,\delta^2}(k,\,z) = \left[\int_{M_{\rm min}}^{M_{\rm max}} dM\ \frac{dn}{dM}b_h(M)\frac{\left\langle N_{g_j}\right\rangle}{\bar{n}_{g_j}}\tilde{v}_g(k\,|M)\right] \times\left[\int_{M_{\rm min}}^{M_{\rm max}} dM\ \frac{dn}{dM}b_h(M)\frac{\tilde{u}(k\,|M)}{\Delta^2}\right]P^{\rm lin}(k). \quad (24)$$

The function $\tilde{u}(k\,|M)$ is the Fourier transform of

$$u(x\,|M) = \rho_h^2(x\,|M)\big/\bar{\rho}^2_{\rm DM} + b_{\rm sub}(M)\ \rho_h(x\,|M)\big/M \times\int d^3x\ \rho_h^2(x\,|M)\Big/\bar{\rho}^2_{\rm DM}, \quad (25)$$

where ρ_h denotes the main halo profile and $b_{\rm sub}$ is the boost function associated to subhalos (introduced above). Note that $\tilde{u}(k=0|M) = (1 + b_{\rm sub}(M,\,z))\ \int d^3x\ \rho^2(x\,|M)\big/\bar{\rho}^2$. The product $\langle N_{g_j}\rangle\ \tilde{v}_g(k\,|m)$ is instead the Fourier transform of $\langle N_{\rm cen,j}(M)\rangle\ \delta^3(x) + \langle N_{\rm sat,j}(M)\rangle\ \rho_h(x\,|M)/M$. We have $\langle N_{g_j}\rangle\ \tilde{v}_g(k=0|m) = \langle N_{g_j}\rangle$. The average number of galaxies g_j at a given redshift is given by $\bar{n}_{g_j}(z) = \int dM\ dn\big/dM\ \langle N_{g_j}\rangle$. The details of the models of $\langle N_{g_j}\rangle$, dn/dM and $\rho_h(x\,|M)$ have been described in the previous sections.

The impact of clustering assumptions on the 3D PS are illustrated in Figure 14(a), where we consider the 2MASS catalog and show $P_{g_j,\delta^2}(k,\,z=0.1)$. The boost from substructures makes the γ-ray contributions from most massive halos to dominate the signal, and this is more pronounced in the HIGH case rather than in the LOW scenario. In the case without substructures, low-mass halos become more important in the total budget of the γ-ray emission. This explains the hierarchy at $k \sim 1\,{\rm Mpc}^{-1}$. For the same reasons, an opposite hierarchy occurs at very small scales ($k \gtrsim 100\,{\rm Mpc}^{-1}$).

In the case of decaying DM, the PS of cross-correlation takes the form

$$P^{1h}_{g_j,\delta}(k,\,z) = \int_{M_{\rm min}}^{M_{\rm max}} dM\ \frac{dn}{dM}\frac{\left\langle N_{g_j}\right\rangle}{\bar{n}_{g_j}}\tilde{v}_g(k\,|M)\,\tilde{v}_\delta(k\,|M) \quad (26)$$

$$P^{2h}_{g_j,\delta}(k,\,z) = \left[\int_{M_{\rm min}}^{M_{\rm max}} dM\ \frac{dn}{dM}b_h(M)\frac{\left\langle N_{g_j}\right\rangle}{\bar{n}_{g_j}}\tilde{v}_g(k\,|M)\right] \times\left[\int_{M_{\rm min}}^{M_{\rm max}} dM\ \frac{dn}{dM}b_h(M)\,\tilde{v}_\delta(k\,|M)\right]P^{\rm lin}(k). \quad (27)$$

Here $\tilde{v}_\delta(k\,|M)$ is the Fourier transform of $\rho_h(x\,|M)/\bar{\rho}_{\rm DM}$. In Figure 14(b), we show $P_{g_j,\delta}(k,\,z=0.1)$ (again for the 2MASS case), together with the matter PS derived within our halo model approach. The latter is compared to a revised halofit PS derived from latest high-resolution N-body simulations (Takahashi et al. 2012). They agree within 20% at $k < 10\,{\rm Mpc}^{-1}$ and this supports our choices for the halo model ingredients. At larger k there is a departure, with less power in the halo model, but the picture at such small scales is in any case very uncertain, also from the simulations point of view.

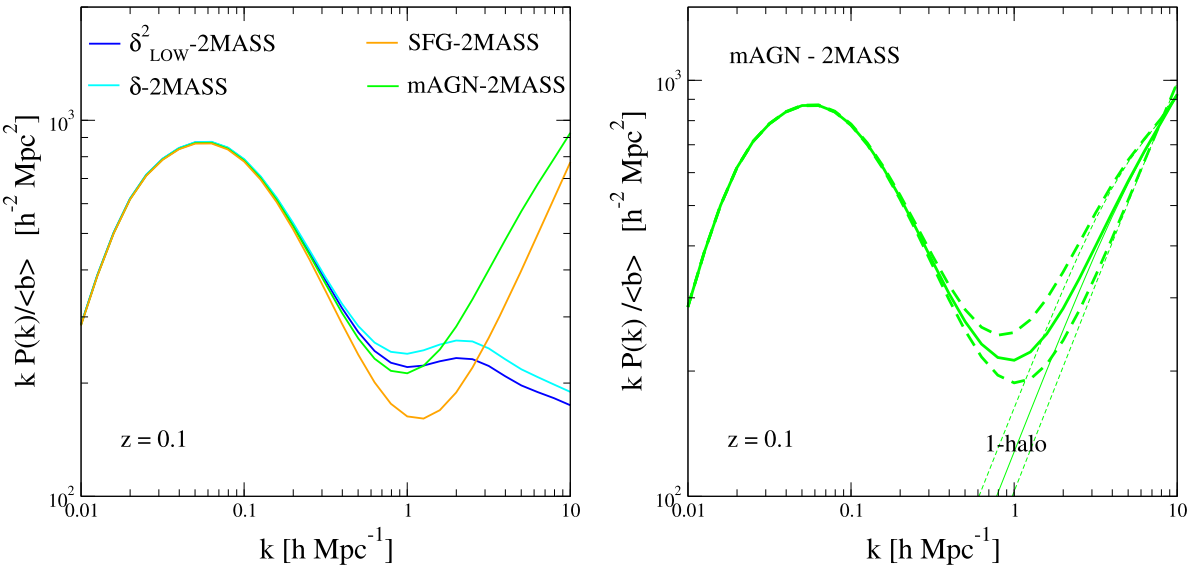

Figure 15. Power spectrum of cross-correlation between γ-ray emitters and 2MASS galaxies at redshift $z = 0.1$. The power spectrum is multiplied by k and divided by the effective bias of γ-ray emitters $\langle b(z = 0.1)\rangle$. The left panel compares predictions from annihilating (in the LOW scenario) and decaying DM with the astrophysical models of mAGN and SFG. The right panel focuses on mAGN and reports the power spectrum with three different assumptions for the $M(\mathcal{L})$ relation (taken from Camera et al. 2014). Thin lines show the one-halo part of the power spectrum.

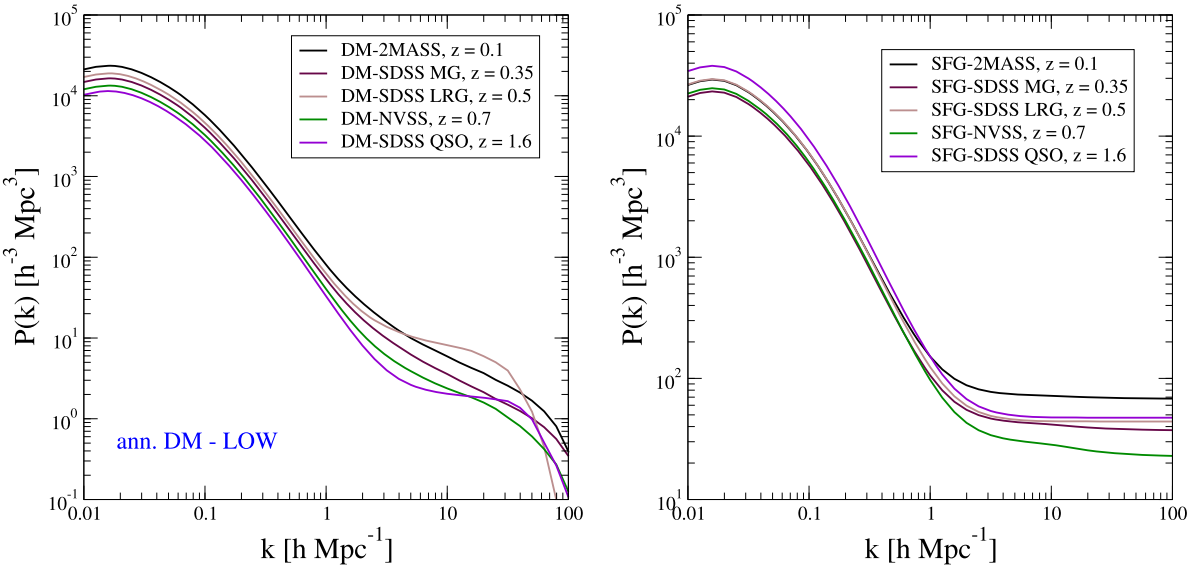

Figure 16. Left: 3D power spectrum of cross-correlation between γ-rays from annihilating DM (in the LOW scenario) and galaxies, evaluated at the redshift corresponding to the peak of the dN_j/dz of each catalog. Right: same as left panel, but for SFG instead of DM.

We assume astrophysical γ-ray emitters to be point-like sources with the density field given by $f_{S_i}(x - x') = \mathcal{L}_{S_i}\,\delta^3(x - x')$. The 3D PS of cross-correlation with galaxy catalogs can be written as

$$P^{1h}_{g_j,S_i}(k,z) = \int_{\mathcal{L}_{\rm min,i}(z)}^{\mathcal{L}_{\rm max,i}(z)} d\mathcal{L}\;\Phi_i(\mathcal{L},z)\,\frac{\mathcal{L}}{\left\langle f_{S_i}\right\rangle}\,\frac{\left\langle N_{g_j}(\mathcal{L})\right\rangle}{\bar{n}_{g_j}}\tilde{v}_g(k|M \tag{28}$$

$$P^{2h}_{g_j,S_i}(k,z) = \left[\int_{\mathcal{L}_{\rm min,i}(z)}^{\mathcal{L}_{\rm max,i}(z)} d\mathcal{L}\;\Phi_i(\mathcal{L},z)\,b_{S_i}(\mathcal{L})\,\frac{\mathcal{L}}{\left\langle f_{S_i}\right\rangle}\right] \times \left[\int_{M_{\rm min}}^{M_{\rm max}} dM\,\frac{dn}{dM}b_h(M)\,\frac{\left\langle N_{g_j}\right\rangle}{\bar{n}_{g_j}}\tilde{v}_g(k|M)\right] \times P^{\rm lin}(k), \tag{29}$$

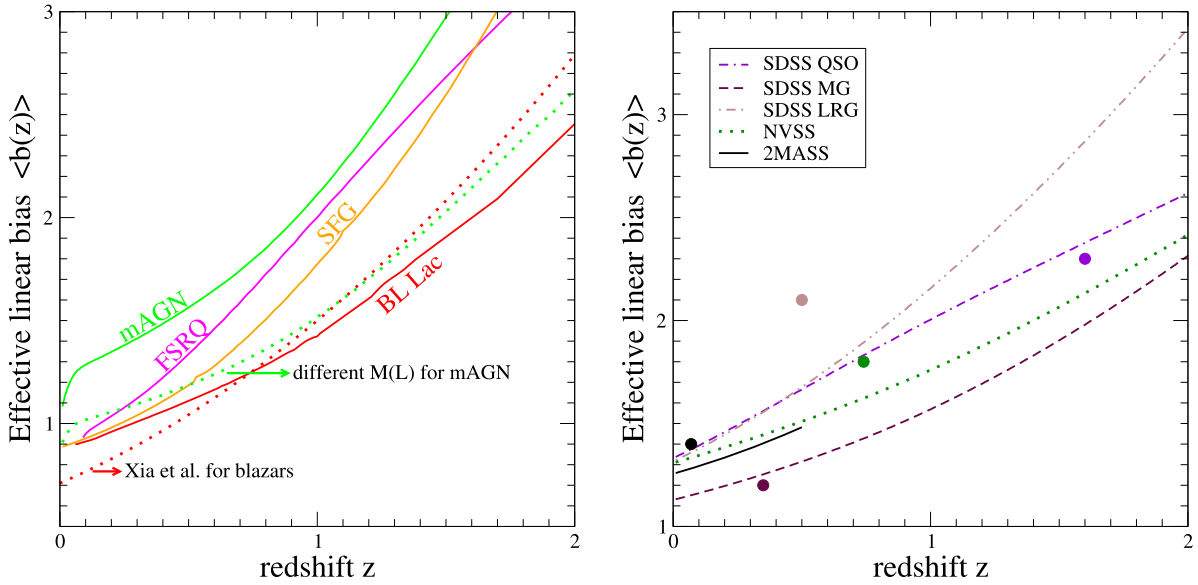

Figure 17. Effective bias for γ-ray astrophysical emitters (left) and galaxies (right), as defined in Equations (30) and (31), respectively. To illustrate the impact of the $M(\mathcal{L})$ description, we additionally show the bias of mAGN when assuming the lower limit discussed in Camera et al. (2014) for such relation (green thin line). For comparison, we also report the bias of γ-ray blazars considered in Xia et al. (2015; red dotted line). In the galaxy cases (right panel), we show with circles the value of the different bias parameters adopted in Xia et al. (2015), where they were taken to be constant in redshift. The position of the dots refers to the redshift which corresponds to the peak of the galaxy distribution dN_j/dz.

where b_{S_i} is the bias of γ-ray astrophysical sources with respect to matter, for which we adopt $b_{S_i}(\mathcal{L}) = b_h(M(\mathcal{L}))$. Both Equations (28) and (29) require the specification of the relation $M(\mathcal{L})$ between the mass of the host halo M and the luminosity of the hosted object $\mathcal{L}$. We will use the modeling of $M(\mathcal{L})$ derived in Camera et al. (2014), where this aspect is discussed, and to which we refer the reader for the details. The blazar $M(\mathcal{L})$ model of Camera et al. (2014) is adopted for both BL Lac and FSRQ.

We caution that Equation (28) for $P^{1h}_{g_j,S_i}$ gives only an approximate estimate of the one-halo correlation. Indeed, modeling the satellite galaxies as a smooth component reduces their correlation with point-like γ-ray sources. On the other hand, we assume that a halo hosting a given γ-ray emitter also hosts the galaxies of all catalogs. This may not be true (e.g., some catalogs are mostly formed by galactic objects which do not host an AGN), thus artificially enhancing $P^{1h}_{g_j,S_i}$. Moreover, Equation (28) is based on average relations, while a relatively small number of outliers (i.e., bright γ-ray sources in a halo with galaxies) can have a relevant impact. For all these reasons, and since $P^{1h}_{g_j,S_i}$ is approximately independent on k, we can include in the fit an arbitrary constant term allowing for both positive and negative corrections to Equation (28). We call this additional quantity the *one-halo correction term*, and we perform the analysis under the assumption that this term is not relevant (i.e., by setting it to vanish) and under the assumption that it is present, leaving it as a free parameter, one for each LSS tracer.

Figure 14 (right panel) shows $P_{g_j,S_i}(k, z = 0.1)$, again taking the 2MASS catalog as illustrative. The different classes of γ-ray emitters show a similar spectrum, and have less (more) power than in the DM cases at intermediate (small) scales, as expected given their size.

In Figure 15, we show the difference between the DM and astrophysical PS at low redshift arising from the one-halo term. To this aim, we divide the PS by the bias in order to have the large-scale PS (i.e., the two-halo term) with a common normalization. At small scales, the power associated with astrophysical sources is larger than for DM. The picture is opposite at intermediate scales, around megaparsec, especially for SFG. The adopted model of $M(\mathcal{L})$ makes the mAGN individual objects that contribute more to mAGN emission to be hosted in relatively large halos. This implies that the mAGN PS at megaparsec scales is similar to the one of DM, explaining (part of) the origin of the degeneracy between mAGN and DM mentioned in the main text. We investigate the impact of different $M(\mathcal{L})$ relations, taken from Camera et al. (2014), in the right panel of Figure 15.

The 3D PS of cross-correlation with the other catalogs are shown in Figure 16. As illustrative examples, we selected the LOW scenario for annihilating DM, and SFG for astrophysical γ-ray sources. The PS are computed at the redshift corresponding to the peak of the dN_j/dz of each catalog.

In Figure 17, we show the effective bias of astrophysical γ-ray emitters and galaxies. They are defined with $P^{2h}_{g_j,S_i} = \langle b_{S_i}\rangle \langle b_{g_j}\rangle P^{\rm lin}$ at $k = 0$, so they read

$$\langle b_{S_i}(z)\rangle = \int_{\mathcal{L}_{\rm min,i}(z)}^{\mathcal{L}_{\rm max,i}(z)} d\mathcal{L}\, \Phi_i(\mathcal{L}, z)\, b_h(M(\mathcal{L}))\, \frac{\mathcal{L}}{\langle f_{S_i}\rangle} \qquad (30)$$

$$\langle b_{g_j}(z)\rangle = \int_{M_{\rm min}}^{M_{\rm max}} dM\, \frac{dn}{dM} b_h(M)\, \frac{\langle N_{g_j}(M)\rangle}{\bar{n}_{g_j}}. \qquad (31)$$

Equation (30) depends on the mass–luminosity relation $M(\mathcal{L})$, while Equation (31) is governed by the modeling of $\langle N_{g_j}(M)\rangle$. The fair agreement shown by the computed bias with findings of auto-correlation studies quoted in the literature (e.g., Zehavi et al. 2005; Ross et al. 2010; White et al. 2011; Ho et al. 2012; Allevato et al. 2014; Reid et al. 2014) is an important check of our modeling of $M(\mathcal{L})$ and $\langle N_{g_j}(M)\rangle$.

The bias of γ-ray blazars appears systematically lower than findings in Allevato et al. (2014). Translating the halo bias in terms of the mean mass hosting the blazars by means of Sheth

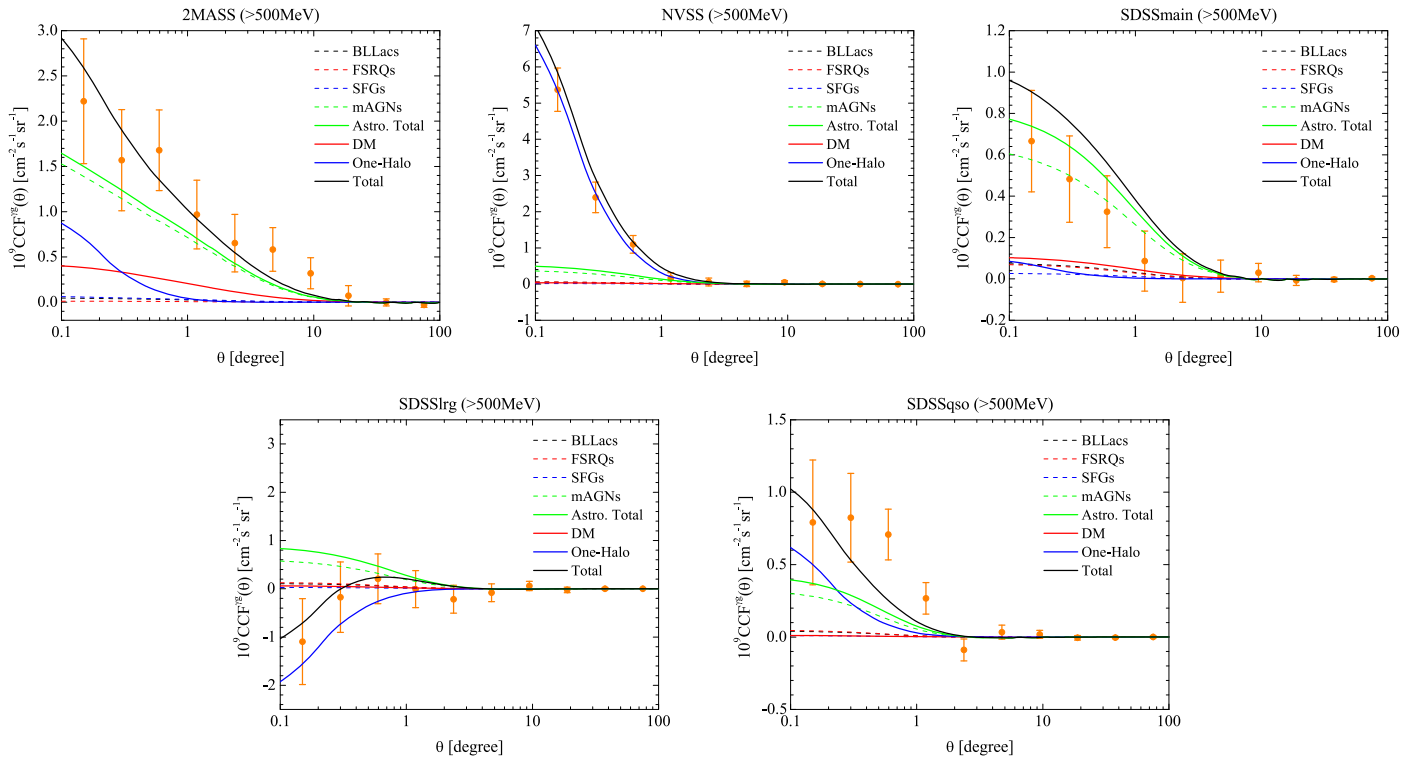

Figure 18. Measured cross-correlation function (CCF; Xia et al. 2015) for $E > 0.5$ GeV, as a function of the angular separation θ in the sky, compared to the best-fit models of this analysis. The contribution to the CCF from the different astrophysical γ-rays emitters (BL Lac, mAGN, SFG, FSRQ) are shown by dashed colored lines, while their sum ("Astro Total") and the DM contribution are indicated by solid green and red lines, respectively. The *one-halo correction term* is shown as a solid blue line. The total contribution to the CCF is given by the black solid line.

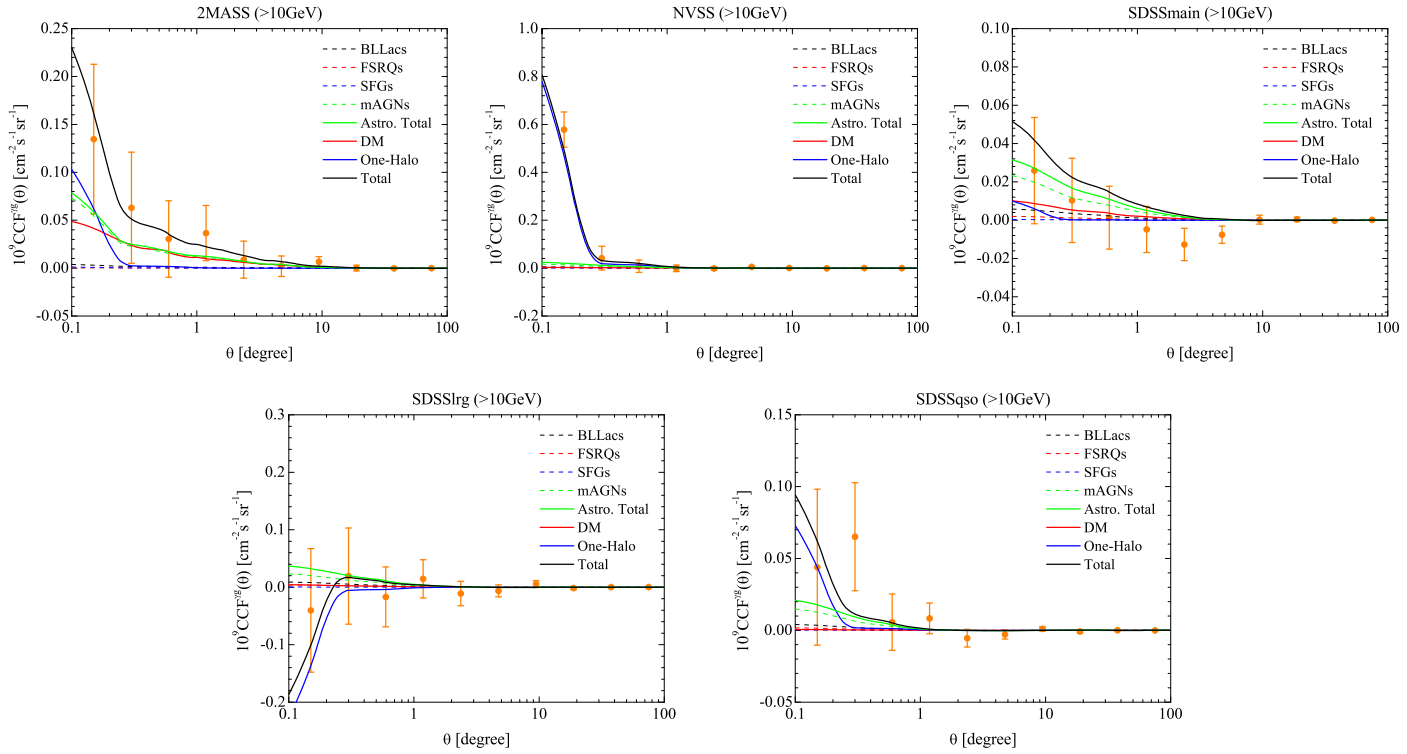

Figure 19. Same as Figure 18 but for $E > 10$ GeV.

& Tormen (1999), their results imply halos of $M \simeq 3 \cdot 10^{13}\, M_{\odot}$, while according to our results shown in Figure 17, FSRQs reside in halos of $M \simeq 1.5 \cdot 10^{13}\, M_{\odot}$ and BL Lacs in $M \simeq 5 \cdot 10^{12}\, M_{\odot}$. This is not surprising if we consider that the work of Allevato et al. (2014) focuses on resolved objects, namely on a blazar subsample given by the

brightest ones, which reside in more massive halos, while on the contrary we investigate the unresolved component, which should be hosted by less massive halos. Moreover, the relatively low number of known γ-ray objects prevents a firm knowledge of their clustering, and sizable uncertainties on the bias are currently present.

APPENDIX D
PLOTS OF CCF AT OTHER ENERGIES

In this appendix, analogous to Figure 5 in the main text, we show the measured cross-correlation function (CCF; Xia et al. 2015) as a function of the angular separation θ in the sky compared to the best-fit models of this analysis for the two energy bands $E > 0.5$ GeV (Figure 18) and $E > 10$ GeV (Figure 19).

REFERENCES

Acero, F., Ackermann, M., Ajello, M., et al. 2015, ApJS, 218, 23
Ackermann, M., Ajello, M., Albert, A., et al. 2012a, PhRvD, 85, 083007
Ackermann, M., Ajello, M., Albert, A., et al. 2015a, ApJ, 799, 86
Ackermann, M., Ajello, M., Allafort, A., Baldini, L., et al. 2012b, ApJ, 755, 164
Ackermann, M., Ajello, M., Atwood, W., et al. 2015b, arXiv:1501.06054
Aihara, H., Allende Prieto, C., An, D., et al. 2011, ApJS, 193, 29
Ajello, M., Gasparrini, D., Sanchez-Conde, M., et al. 2015, ApJL, 800, L27
Ajello, M., Romani, R., Gasparrini, D., et al. 2014, ApJ, 780, 73
Ajello, M., Shaw, M., Romani, R., et al. 2012, ApJ, 751, 108
Allevato, V., Finoguenov, A., & Cappelluti, N. 2014, ApJ, 797, 96
Ando, S. 2014, JCAP, 10, 61
Ando, S., Benoit-Lévy, A., & Komatsu, E. 2014, PhRvD, 90, 023514
Ando, S., & Komatsu, E. 2013, PhRvD, 87, 123539
Ando, S., & Pavlidou, V. 2009, MNRAS, 400, 2122
Atwood, W. B., Abdo, A. A., Ackermann, M., et al. 2009, ApJ, 697, 1071
Berlind, A. A., & Weinberg, D. H. 2002, ApJ, 575, 587
Bilicki, M., Jarrett, T. H., Peacock, J. A., Cluver, M. E., & Steward, L. 2014, ApJS, 210, 9
Blake, C., & Wall, J. 2002, MNRAS, 337, 993
Calore, F., Di Mauro, M., Donato, F., & Donato, F. 2014, ApJ, 796, 1
Camera, S., Fornasa, M., Fornengo, N., & Regis, M. 2013, ApJL, 771, L5
Camera, S., Fornasa, M., Fornengo, N., & Regis, M. 2014, arXiv:1411.4651
Chatterjee, S., Degraf, C., Richardson, J., et al. 2012, MNRAS, 419, 2657
Cooray, A., & Sheth, R. K. 2002, PhR, 372, 1
Cuoco, A., Brandbyge, J., Hannestad, S., Haugboelle, T., & Miele, G. 2008, PhRvD, 77, 123518
Cuoco, A., Komatsu, E., & Siegal-Gaskins, J. 2012, PhRvD, 86, 063004
Di Mauro, M., Calore, F., Donato, F., Ajello, M., & Latronico, L. 2014a, ApJ, 780, 161
Di Mauro, M., Cuoco, A., Donato, F., & Siegal-Gaskins, J. M. 2014b, JCAP, 1411, 021
Di Mauro, M., Donato, F., Lamanna, G., Sanchez, D., & Serpico, P. 2014c, ApJ, 786, 129
Efstathiou, G. 2004, MNRAS, 349, 603
Fichtel, C. E., Kniffen, D. A., & Hartman, R. C. 1973, ApJL, 186, L99
Fornasa, M., & Sanchez-Conde, M. A. 2015, PhR, 598, 1
Fornasa, M., Zavala, J., Sanchez-Conde, M. A., et al. 2013, MNRAS, 429, 1529
Fornengo, N., Perotto, L., Regis, M., & Camera, S. 2014, arXiv:1410.4997
Fornengo, N., & Regis, M. 2014, FrP, 2, 6
Franceschini, A., Rodighiero, G., & Vaccari, M. 2008, A&A, 487, 837
Gao, L., Frenk, C., Jenkins, A., Springel, V., & White, S. 2012, MNRAS, 419, 1721
Gómez-Vargas, G. A., Cuoco, A., Linden, T., et al. 2014, NIMPA, 742, 149
Gruppioni, C., Pozzi, F., Rodighiero, G., et al. 2013, MNRAS, 432, 23
Hickox, R. C., & Markevitch, M. 2007, ApJL, 661, L117
Ho, S., Cuesta, A., Seo, H.-J., et al. 2012, ApJ, 761, 14
Inoue, Y. 2011, ApJ, 733, 66
Jarrett, T., Chester, T., Cutri, T., et al. 2000, AJ, 120, 298
Kaiser, N. 1992, ApJ, 388, 272
Kaiser, N. 1998, ApJ, 498, 26
Keshet, U., Waxman, E., & Loeb, A. 2004, JCAP, 4, 6
Kraushaar, W. L., Clark, G. W., Garmire, G. P., et al. 1972, ApJ, 177, 341
Laureijs, R. 2009, arXiv:0912.0914
Lewis, A., & Bridle, S. 2002, PhRvD, 66, 103511
Limber, D. N. 1953, ApJ, 117, 134
Mayer-Hasselwander, H. A., Kanbach, G., Bennett, K., et al. 1982, A&A, 105, 164
McIntosh, D. H., Bell, E. F., Weinberg, M. D., & Katz, N. 2006, MNRAS, 373, 1321
Navarro, J. F., Frenk, C. S., & White, S. D. 1997, ApJ, 490, 493
Ng, K. C. Y., Laha, R., Campbell, S., et al. 2014, PhRvD, 89, 083001
Nolan, P. L., Abdo, A. A., Ackermann, M., et al. 2012, ApJS, 199, 31
Padovani, P., Ghisellini, G., Fabian, A. C., & Celotti, A. 1993, MNRAS, 260, L21
Planck Collaboration, Ade, P. A. R., Aghanim, N., et al. 2015, arXiv:1502.01589
Prada, F., Klypin, A. A., Cuesta, A. J., Betancort-Rijo, J. E., & Primack, J. 2012, MNRAS, 428, 3018
Regis, M., Xia, J.-Q., Cuoco, A., et al. 2015, PRL, 114, 241301
Reid, B. A., Seo, H.-J., Leauthaud, A., Tinker, J. L., & White, M. 2014, MNRAS, 444, 476
Richards, G. T., Myers, A. D., Gray, A. G., et al. 2009, ApJS, 180, 67
Richardson, J., Zheng, Z., Chatterjee, S., Nagai, D., & Shen, Y. 2012, ApJ, 755, 30
Ross, A. J., Percival, W. J., & Brunner, R. J. 2010, MNRAS, 407, 420
Sanchez-Conde, M. A., & Prada, F. 2014, MNRAS, 442, 2271
Sheth, R. K., & Tormen, G. 1999, MNRAS, 308, 119
Shirasaki, M., Horiuchi, S., & Yoshida, N. 2014, PhRvD, 90, 063502
Siegal-Gaskins, J. M., Reesman, R., Pavlidou, V., Profumo, S., & Walker, T. P. 2011, MNRAS, 415, 1074
Sreekumar, P., Bertsch, D. L., Dingus, B. L., et al. 1998, ApJ, 494, 523
Stecker, F. W., & Salamon, M. H. 1996, ApJ, 464, 600
Strong, A. W., Moskalenko, I. V., & Reimer, O. 2004, ApJ, 613, 956
Takahashi, R., Sato, M., Nishimichi, T., Taruya, A., & Oguri, M. 2012, ApJ, 761, 152
Tamborra, I., Ando, S., & Murase, K. 2014, JCAP, 1409, 043
The Dark Energy Survey Collaboration 2005, arXiv:astro-ph/0510346
White, M., Blanton, M., Bolton, A., et al. 2011, ApJ, 728, 126
Xia, J.-Q., Cuoco, A., Branchini, E., Fornasa, M., & Viel, M. 2011, MNRAS, 416, 2247
Xia, J.-Q., Cuoco, A., Branchini, E., & Viel, M. 2015, ApJS, 217, 15
Zehavi, I., Zheng, Z., Weinberg, D. H., et al. 2005, ApJ, 630, 1
Zheng, Z., Berlind, A. A., Weinberg, D. H., et al. 2005, ApJ, 633, 791